Title: **Maternal-fetal immune conflict contributes to male-specific impairments in a mouse model of neurodevelopmental disorders**

Authors: Irene Sanchez-Martin[1], Bharti Kukreja[2], Paige Henderson[1], Qianyu Lin[1], Daniel DiMartino[1], Valerie Bagan[1], Justin Park[1], Brian T. Kalish[2,3], and Lucas Cheadle[1,4*]

Affiliations:

[1]Cold Spring Harbor Laboratory; Cold Spring Harbor, NY, 11724, USA.

[2]Division of Newborn Medicine, Boston Children's Hospital; Boston, MA, 02115, USA.

[3]F.M. Kirby Neurobiology Center, Boston Children's Hospital; Boston, MA, 02115, USA.

[4]Howard Hughes Medical Institute; Cold Spring Harbor, NY, 11724, USA.

*Corresponding author. Email: cheadle@cshl.edu

Abstract:

Autism spectrum disorder (ASD) arises through a combination of genetic and environmental risk factors. One environmental risk factor is maternal immune activation (MIA), wherein pathogenic infections in pregnant individuals increase the risk of ASD in the offspring, an effect seen most prevalently in males. However, the reasons that males exhibit this heightened sensitivity to MIA, and the mechanisms through which inflammatory signals traverse the maternal-fetal interface to impact the developing male embryo, remain largely mysterious. Here, we harness the poly(I:C) mouse model of neurodevelopmental disorders to uncover changes in fetal health and in the structure and composition of the maternal-fetal interface that occur within twenty-four hours of MIA. We find that 30% of embryos exhibit large-scale teratogenic abnormalities—ranging from decreased fetal weight to a lack of external sensory organ development—while 70% of embryos develop normally. Strikingly, these abnormalities only occur in a subset of males, and never in females. Single-nucleus transcriptomics revealed the robust induction of pro-inflammatory gene programs across the placentas of males exhibiting deficits following MIA, including in immune, vascular, and decidual cells. These transcriptomic changes were particularly prominent in spongiotrophoblasts, fetally derived cells that in part comprise the border between the maternal and fetal compartments of the placenta. While upregulating inflammatory pathways following MIA, spongiotrophoblasts simultaneously downregulate extracellular matrix and hormone biosynthesis pathways, concurrent with a breakdown in the structural integrity of the placenta and the accumulation of immune cells and cytokines in the embryo's amniotic fluid. One of these cytokines, IL-6, is necessary for the emergence of MIA-evoked developmental abnormalities. Our data suggest that MIA induces a rapid transition from an immunosuppressive toward a pro-inflammatory maternal-fetal interface in a subset of male embryos, leading to acute developmental deficits that are restricted to this vulnerable cohort. These data suggest that male embryos may harbor unique proteins capable of eliciting an inflammatory response at the maternal-fetal interface that, when coupled with a loss of immunosuppression due to maternal infection, derails embryonic development selectively in males.

Main Text:

Autism spectrum disorder (ASD) is a heterogeneous class of neurodevelopmental conditions characterized by cognitive and social impairments that arises in early childhood and persists across the lifespan. ASD prevalence has increased substantially over recent decades, underscoring its growing impact on public health(*1-3*). A striking feature of ASD is that, while genetic factors play a strong role(*4*), environmental factors such as prenatal inflammation also contribute to neurodevelopmental dysfunction in a subset of individuals. For example, pathogenic infections during pregnancy can activate maternal immune pathways that disrupt fetal neurodevelopment, increasing ASD risk in offspring by approximately three-fold(*5-8*). Despite this association, how a transient inflammatory insult during gestation compromises brain function across the lifespan remains poorly understood.

While prenatal inflammation is a major risk factor for ASD, the majority of fetuses exposed to inflammation in the womb undergo neurotypical development. This suggests that vulnerability to MIA is restricted to a subset of the population. For example, males appear disproportionately affected, consistent with the 4:1 male bias in ASD diagnoses(*9*). While the reasons that males are more susceptible to prenatal inflammation are a topic of debate, one possibility is that male fetuses express paternally derived proteins that could cause the maternal immune system to tolerate the semi-allogeneic male fetus less well than the fetuses of females(*10, 11*). In turn, this loss of immune tolerance could disrupt neuro-immune homeostasis in the fetus. However, while this hypothesis is compelling, the factors that underlie the increased susceptibility of males to MIA remain to be established.

Mouse models of MIA have been instrumental in linking prenatal inflammation to ASD-relevant outcomes(*12*). A widely used paradigm involves administration of the viral mimetic poly(I:C) during midgestation. Prior work has focused primarily on behavioral consequences in adult offspring, unveiling ASD-relevant phenotypes including decreased sociability, an overabundance of repetitive behaviors, and heightened anxiety compared to saline-treated control mice(*13-16*). However, while a handful of studies have identified an increase in inflammatory cytokines at the maternal-fetal interface several days following exposure to poly(I:C)(*17-20*), few studies have explored the earliest changes that give rise to these deficits *in utero*. Here, we harness the $\text{MIA}_{\text{poly(I:C)}}$ model to shed light on the factors that underlie the susceptibility or resilience of individual embryos to MIA, uncovering evidence that maternal immune conflict with male embryos contributes to male-specific developmental deficits in this model of ASD. Our results lay the groundwork for studies that could inform the development of strategies for preventing or treating ASD in prenatal males.

Results:

To uncover the mechanisms linking maternal inflammation to neurodevelopmental dysfunction, we adopted the $\text{MIA}_{\text{poly(I:C)}}$ mouse model. In this model, pregnant mice are intraperitoneally administered 20 mg/kg of poly(I:C), a synthetic double stranded RNA that predominantly (but not exclusively) binds Toll-like receptor 3 (TLR3) to induce the same innate immune pathways as a viral infection(*21, 22*). Administration of poly(I:C) (or saline as control) occurs at E12.5, a gestational timepoint that correlates with the late second trimester in humans when maternal infections have been linked to ASD in the offspring(*23, 24*). Yet, while the impact of prenatal inflammation on the adult offspring of $\text{MIA}_{\text{poly(I:C)}}$ mice has been broadly assessed at the behavioral level, the initial mechanisms by which maternal inflammation triggers life-long deficits in brain function in the fetus remain largely unknown.

MIA elicits large-scale developmental abnormalities in a subset of embryos within 24 hours of poly(I:C) exposure

To identify the earliest effects of MIA on fetal development, we administered poly(I:C) or saline to pregnant C57B/6J dams at E12.5 then harvested the embryos 24 hours later (i.e. E13.5; Fig. 1A). Since MIA models exhibit substantial variability in their activation of the maternal immune system depending upon factors ranging from the mouse strain to the commercial source of poly(I:C)(*25-27*), we validated induction of inflammation in all dams used in the study by performing ELISAs to ensure that levels of IL-6 in the maternal blood are induced following poly(I:C) injection (Fig. 1B,C). Twenty-four hours later at E13.5, we harvested embryos, then applied a systematic battery of morphological measurements to assess differences between the groups. While embryos harvested from saline-treated mice closely resembled those of uninjected wild-type mice (Fig. S1A), embryos from poly(I:C)-treated dams displayed significant abnormalities. These abnormalities included changes in overall weight and morphology (Fig. 1D-I), craniofacial and head malformations such as decreased lambda-to-bregma distance (Fig. 1J-L), evidence of a lack of vascular integrity on the surface of the embryo (Fig. 1M), a lack of external sensory organ (i.e. ear pavilion and whisker pad) development (Fig. 1N), and abnormalities in spine and tail morphology (Fig. 1O). Although these differences between groups were statistically significant, the distributions of the data overlap substantially, suggesting that some fetuses were deleteriously impacted by MIA while others maintained a normal developmental trajectory. Thus, we next quantified the proportions of embryos per litter displaying at least one of these abnormalities between saline and poly(I:C) groups. Consistent with the partial overlap between the data distributions, we found that about 30% of embryos displayed one or more developmental abnormalities following MIA, versus 0% of embryos from the control group (Fig. 1P). Importantly, we observed the same effects when we applied the $\text{MIA}_{\text{poly(I:C)}}$ paradigm to the BALB/c mouse strain, indicating that, while untested mouse strains may respond to MIA differently(*28*), our observations are not limited to mice of a single genetic background (Fig. S1B,C).

MIA-induced deficits in embryonic development are restricted to a subpopulation of male embryos

As individual embryos were differentially affected by MIA, we next classified the embryos of poly(I:C)-treated dams into three categories based upon the changes observed. Embryos were classified as those appearing indistinguishable from healthy controls (*normal*, $\text{poly(I:C)}^{\text{norm}}$), those exhibiting at least one developmental abnormality but not showing signs of reabsorption (*moderate*, $\text{poly(I:C)}^{\text{mod}}$), and those exhibiting extreme deficits which included signs of reabsorption, indicating that these embryos likely undergo intrauterine demise prior to birth (*strong*, $\text{poly(I:C)}^{\text{strong}}$; Fig. 2A). To provide unbiased justification for this classification system, we performed a multiple correspondence analysis (MCA) using a panel of phenotypic descriptors encoded as binary indicators. This analysis shows a clear, graded separation of embryos into these three phenotypic groups along two dimensions. Dimension 1 captures the severity gradient such that $\text{poly(I:C)}^{\text{strong}}$ cases cluster with traits like head and limb abnormality and absence of ears and whiskers. $\text{Poly(I:C)}^{\text{norm}}$ embryos cluster at the opposite end, and $\text{poly(I:C)}^{\text{mod}}$ embryos are distributed between these two groups. This three-level classification reflects how anomalies co-occur in patterns rather than in isolation, preserving the main multivariate structure while remaining interpretable, and enabling consistent downstream comparison between phenotypes (Fig. 2B). These results are consistent with the observation that pathogenic infection in humans impacts fetal development heterogeneously, as well as the known link between prenatal inflammation and stillbirth.

We harnessed this classification system to identify factors that render some embryos susceptible to teratogenic deficits in response to MIA while others remain resilient. Since we inject poly(I:C) into the lower right quadrant of the dam's abdomen, we first considered the possibility that embryos closest to the injection site are exposed to a greater concentration of inflammatory factors, thereby causing these embryos to undergo developmental changes more readily. However, we did not observe a significant correlation between phenotypic severity and the locus of injection (Fig. S2A,B).

We next considered the possibility that, even at this early developmental timepoint, the sex of the embryo might influence susceptibility to MIA. We used PCR to detect the Y chromosome genes *Rbm31 and SRY* in poly(I:C)-exposed embryos across phenotypes (Fig. S2C). Strikingly, while the unaffected poly(I:C)^{norm} group included both male and female embryos, 100% of embryos within the poly(I:C)^{mod} and poly(I:C)^{strong} groups were male. Thus, roughly 60% of male fetuses from MIA dams exhibit some combination of developmental deficits at E13.5 compared to 0% of females (Fig. 2C). When plotted by litter, we find that on average about 30% of male embryos within a given litter exhibit deficits, although the distribution is wide, with some litters including no impacted embryos while others contain greater than 60% affected male embryos (Fig. 2D). The deleterious effect of MIA on male but not female embryonic development in C57Bl/6J mice occurs in BALB/c mice as well (Fig. S3). This finding is intriguing given the strong sex bias in disorders such as ASD, where males are more likely to receive a diagnosis than females at a ratio of 4:1(*9*). Thus, sex (but not intrauterine position) is one factor underlying risk of embryonic developmental dysfunction following MIA.

We next considered the possibility that the proximity of a male embryo to other embryos in the womb might influence its phenotype, as this relationship was recently shown to impact behavioral outcomes of MIA offspring(*29*). We found that embryos were significantly more likely to fall within the poly(I:C)^{mod} group (versus the poly(I:C)^{norm} group) if they were neighbored by one or two other male embryos than if they were surrounded by females. A similar pattern emerged for fetuses within the poly(I:C)^{strong} group (Fig. 2E,F). Thus, at least two factors underlie the selective susceptibility of a fetus to early developmental dysfunction in MIA: the sex of the fetus, and the sexes of neighboring fetuses in the womb.

Inducing MIA after the placenta matures fails to elicit developmental deficits

Prior work in mouse models of MIA suggests that the effects of poly(I:C) exposure on neurodevelopment can vary depending upon the stage of prenatal development at which inflammation is induced(*30*). Thus, we next asked whether E12.5 - E13.5 represents a period of development when some fetuses are particularly sensitive to inflammation. In support of this idea, when we injected poly(I:C) at E14.5 (when the placental barrier is mature), then assessed embryos at E15.5, fetal development was generally unaffected in both males and females (Fig. S4A-C). Conversely, inducing MIA at E9.5 led to developmental abnormalities or intrauterine demise in embryos of both sexes (Fig. S4D-F). These data suggest that the developmental age at which MIA occurs strongly influences its impact on fetal development, and that E12.5-E13.5, during which the placental barrier is still being established, is a sensitive period of susceptibility of some male fetuses to MIA.

The extracellular matrix is compromised in the placentas of poly(I:C)^{mod} embryos

C57Bl/6J mice typically carry litters of four to eight embryos at once, and each embryo harbors a unique maternal-fetal interface in the form of the placenta. The placenta is comprised of three layers: (1) the decidua which is derived from the uterus and is thus of maternal origin; (2) the fetally-derived spongiotrophoblast (SpT) layer which harbors the junctional zone, where maternal and fetal compartments of the placenta meet; and (3) the labyrinth, where maternal and fetal blood vessels intermingle and exchange nutrients, hormones, and cytokines (Fig. 3A). Given that poly(I:C) exposure induces developmental deficits in a subset of male embryos when the placenta is still maturing (E12.5) but not after the placental barrier is fully established (E14.5), we hypothesized that MIA-induced changes in the placenta underlie the phenotypes we observe. To test this hypothesis, we performed bulk RNA-sequencing on the placentas of saline-treated male embryos and poly(I:C)-treated embryos that displayed developmental deficits without signs of reabsorption (i.e. the poly(I:C)^{mod} population; Fig. S5A). We find that genes encoding extracellular matrix (ECM) proteins, particularly those in the collagen (e.g. *ColGalT2*, *Col15a1, Col16a1, Col27a1, and Col12a1*) and laminin (*Lama3*, *Lamb3*, and *Lamc3*) families show reduced expression in poly(I:C)^{mod} embryos compared to control*s* (Fig. S5B,C). Our data suggest that the ECM is compromised in the placentas of male embryos that exhibit deficits in response to MIA.

Single-nucleus RNA sequencing reveals cell type-specific vulnerabilities of the male placenta to MIA

While informative, bulk RNA-sequencing lacks the resolution to identify which components of the placenta are compromised following MIA. Thus, we performed single-nucleus RNA-sequencing (snRNAseq) to identify the placental cell types that may be particularly sensitive to poly(I:C). We mapped gene expression differences between placentas associated with poly(I:C)^{mod} versus male controls across 20 distinct cell types annotated based upon prior literature(*31, 32*). We grouped cell types into the following categories (genes enriched in each class are shown in brackets): (1) cells that make up the structural fabric of the placenta and support fetal health and growth (decidual cells [*Prl8a2*, *Cryab*], two clusters of SpTs [*Taf7l*], glycogen cells [*Plac8*, *Igfbp7*], two clusters of epithelial cells [*Mecom*, *Cubn*], and parietal endoderm cells [*Lama1*, *Lamb1*]); (2) precursors that give rise to these cell types (SpT precursors [*Prl2c3*], syncytiotrophoblast precursors [*Epha4*,low *Ctsq*],and junctional zone precursors [*Prune2*]); (3) cells associated with the vasculature (sinusoidal trophoblast giant cells [*Ctsq*, *Lepr*, *Nos1ap*], syncytiotrophoblasts I [*Tfrc*], syncytiotrophoblasts II [*Slc13a4*, *Synb*], erythrocytes [*Hbb-y*], mesenchymal [*Col1a1*, *Col1a2*], endothelial cells [*Pecam1*], and maternally derived veinous endothelial cells [*Hdac9*]), and (4) immune cells (one cluster of maternally derived *Ptprc* + cells, one cluster of fetally derived [*Afp*] *Ptprc*+ immune cells, and one cluster of uterine natural killer cells [*Pbx1*, *Pgr*]; Fig. 3B). The final dataset includes 197,237 nuclei passing a stringent QC pipeline in which unhealthy or dying cells, doublets, and ambient RNA were removed (Fig. S6).

To shed light on large-scale changes occurring within the placenta following MIA, we first asked whether the cellular composition of saline-exposed male and poly(I:C)^{mod} placentas differed by calculating the proportionality of cells across all types in both conditions. We find that several populations of fetally-derived cells that make up the middle layer of the placenta and share a developmental origin (SpT precursors, two populations of SpTs, glycogen cells [GCs], and junctional zone precursors) are significantly more abundant in poly(I:C)^{mod} placentas versus controls (Fig. 3C). To validate this upregulation, we quantified trophoblast giant cells (TGCs), identified based on their large size, within both conditions. TGCs are a terminally differentiated cell type derived from SpT progenitors that make up the junctional zone, the physical boundary between the maternal and fetal placental compartments. As suggested by snRNAseq data, we find that TGCs are significantly more abundant in poly(I:C)^{mod} placentas than in controls (Fig. 3D,E). In contrast, other cell types, including immune cells as well as cells involved in nutrient exchange between maternal and fetal blood vessels (uterine natural killer [uNK] cells, sinusoidal trophoblast giant cells [S-TGCs, syncitiotrophoblasts [SynTI], fetally derived immune cells, endothelial cells, mesenchymal cells, and parietal endoderm cells) are less abundant in poly(I:C)^{mod} placentas (Fig. 3C). This suggests that the fetally-derived SpT lineage is expanded in the placentas of mice that exhibit developmental abnormalities in response to MIA. Conversely, cells that mediate interactions between maternal and fetal blood vessels within the highly vascularized placental labyrinth as well as uNK cells are present at lower levels following MIA, suggesting compromised nutrient and cytokine exchange.

Next, we applied differential gene expression analysis to uncover transcriptomic changes elicited by MIA. For every cell type, we observed robust transcriptomic shifts meeting a highly stringent threshold of 4.0 absolute fold change and FDR < 0.05 between poly(I:C)^{mod} and saline-treated male placentas, suggesting multi-cellular disruption arising within 24 hours of a single dose of poly(I:C) (Fig. 3F). Interestingly, the majority of differentially expressed genes (DEGs) for most cell types were downregulated rather than upregulated by MIA, potentially suggesting a generalized blunting of cellular function. These data suggest that transcriptomic changes occur in most cell types within the placentas of a vulnerable subpopulation of male embryos within 24 hours of exposure to MIA.

Transcriptional pathways induced by MIA reflect inflammation and antigenicity

We first asked how immune cell populations respond to poly(I:C) exposure, beginning with maternally derived immune cells (immune_1 cluster and uterine natural killer cells). Genes upregulated by poly(I:C) in immune cluster 1 are highly enriched for mediators of programmed cell death. In particular, these cells upregulate several genes in the granzyme family of apoptosis-inducing secreted enzymes (e.g. *Gzmf*, *Gzmg*, *Gzmd*, *Gzme*, and *Gzmc*) which play an important role in the removal of damaged cells in response to inflammation, and have been previously associated with MIA(*33*). Concurrently, in response to poly(I:C), maternally-derived immune cells dampen expression of genes associated with pregnancy, such as prolactin-like hormones (e.g. *Prl3b1*, *Prl7d1*, *Prl2c5*, *Prl7a1*, *Prl2c3*, *Prl2c2*, and *Xbp1*), endocrine signals that are necessary for promoting maternal immunotolerance of the fetus (Fig. 3G)(*34*). Uterine NK (uNK) cells also significantly blunt prolactin-like hormone signaling in response to MIA, while upregulating pro-inflammatory myeloid cell-related genes such as the complement component C3 and other aspects of type two immunity. These cells also induce factors involved in antigen processing and presentation (e.g. H2-K1, H2-Q7), suggesting the possibility of an early adaptive immune response. Thus, maternally derived immune cells exhibit significant immune activation in the placentas of poly(I:C)^{mod} embryos.

In contrast to maternally derived immune cells, MIA did not induce cell death pathways in fetally-derived immune cells (immune_2 cluster), but rather induced genes involved in cell recruitment and migration. For example, genes induced in these cells by MIA include the chemotactic cues *Cxcl2* (also known as MIP-2a) and *Cxcl10* (also known as IP-10) which play key roles in recruiting immune cells to sites of inflammation. Furthermore, members of the classical complement cascade (e.g. *C3)* are induced in fetally-derived immune cells by poly(I:C). Conversely, genes involved in lysosomal function, such as the Cathepsin family, are decreased in fetally-derived immune cells along with a blunting of prolactin-like hormone signaling as observed in maternal immune cells as well (Fig. 3H,I). Thus, MIA leads to the induction of pro-inflammatory pathways in both maternally and fetally derived immune cells, with maternally derived cells inducing cell death via granzyme production and fetally derived cells recruiting granulocytes and other immune populations to the fetal placenta.

Following poly(I:C) exposure, maternally-derived decidual cells also upregulate genes associated with a strong immune response to MIA, similarly to maternally derived immune cells. These cells induce mediators of antigen processing and presentation (e.g. *H2-K1*, *H2-D1*, *H2-Q7*) following MIA similar to uNK cells (Fig. 3J). These results are consistent with poly(I:C) directly activating decidual cells as previously reported(*35*). In addition to mounting a potentially antigenic response, decidual cells upregulate factors such as *Aqp1* and *Serpine1* which promote angiogenesis, and dampen the expression of genes associated with cellular motility and migration (e.g. *Amot* and *Kitl*) (Fig. 3J). These data suggest that a switch from a pregnancy-supporting, immunosuppressive microenvironment toward an inflammatory transcriptomic state characterizes the responses of both maternally- and fetally-derived placental cells to MIA.

Genes encoding the extracellular matrix and immunosuppressive hormones are decreased in spongiotrophoblasts following MIA

Bulk RNA-sequencing suggests that the ECM is significantly compromised in the placentas of poly(I:C)^{mod} mice (Fig. S5), but the cell types contributing to this dysregulation are not clear. Our snRNAseq analysis addresses this question, revealing that SpTs are a primary cell type contributing to the loss of the ECM in the context of MIA. Specifically, SpTs decrease expression of several collagen (e.g. *Col1a1*, *Col1a2*, *Col12a1*) and laminin (e.g. *Lama2*, *Lama3*, and *Lama4*) family members following MIA, consistent with the results of our bulk RNA-seq analysis (Fig. 4A,B).

To validate this observation at the protein level, we performed immunofluorescence for Col1a1 in the placentas of males from control and poly(I:C)-treated dams representing all phenotypes: poly(I:C)^{norm} (no deficits), poly(I:C)^{mod} (moderate deficits), and poly(I:C)^{strong} (extreme deficits that can progress to reabsorption). We observe significant decreases in collagen deposition in male embryos from poly(I:C)^{mod} and poly(I:C)^{strong} groups, while collagen levels were intact in poly(I:C)^{norm} embryos which lacked developmental deficits (Fig. 4C,D). Thus, the placental ECM is dramatically compromised following MIA, but only in male embryos that exhibit developmental deficits, suggesting a direct link between the transcriptomic changes we observe in the placenta and the severity of the developmental abnormalities observed in the fetuses.

In addition to a decrease in ECM components, in response to MIA, SpTs joined several other cell types in exhibiting significantly decreased expression of transcripts involved in hormone biosynthesis and signaling (Fig. 4A,E). Whereas in immune cells most of the hormone-associated gene changes involve a dampening of prolactin-like hormones, SpTs strongly decrease their expression of *Hsd17b2* and *Cyp11a1*, both of which are involved in the biosynthesis of progesterone and testosterone, by over 8-fold. MIA also led to robust decreases in the expression of the progesterone receptor (*Pgr*) and estrogen receptor alpha (*Esr1*), which might be a compensatory response to the lower abundance of these hormones in general (Fig. 4A,E). Altogether, these data suggest that the dampening of ECM production and hormone signaling in fetally-derived SpT-lineage cells contributes to a loss of placental integrity at the junctional zone.

A subpopulation of placental SpTs expressing high levels of glycoproteins is expanded in MIA

Consistent with SpTs being highly sensitive to poly(I:C) exposure, a subpopulation of SpTs, which we term $\mathrm{SpT_{MIA}}$ cells, is expanded in the placentas of $\mathrm{poly(I{:}C)^{mod}}$ embryos. These cells, which cluster distinctly from the largest SpT cluster described above, are twice as abundant in $\mathrm{poly(I{:}C)^{mod}}$ placentas as controls (Fig. 3B,C). Furthermore, differential gene expression analysis revealed that $\mathrm{SpT_{MIA}}$ cells induce remarkably high levels of two related classes of Ig-superfamily glycoproteins following MIA: pregnancy-specific glycoproteins (Psgs; *Psg27*, *-28*, *-21*, *-29*, *-19*, *-23*, *-25*, *-18*, *-17*, *-16*, *-22*, and *-26*) and Carcinoembryonic antigen-related cell adhesion molecules (Ceacams; *Ceacam3*, *-11*, *-5*, *-9*, *-14*, *-12*, *-13*, and *-1*)(Fig. 4F,G). While not widely studied in mice, work on the human placenta suggests that both classes of proteins can suppress maternal inflammation to protect the fetus during gestation(*36-39*). Interestingly, the two SpT populations in our dataset (SpT and $\mathrm{SpT_{MIA}}$) differ in their transcriptomic responses to MIA, as the largest cluster of SpTs decreases *Psg23* expression with only the smaller population of $\mathrm{SpT_{MIA}}$ cells increasing it. In line with this result, multiplexed fluorescence *in situ* hybridization for the SpT marker *Ascl2* and *Psg23* in placental sections revealed a lower percentage of *Psg23*-expressing SpTs in $\mathrm{poly(I{:}C)^{mod}}$ versus control males (Fig. S7A,B). These results implicate Psgs and Ceacams in the placental response to MIA, although whether these factors contribute to developmental deficits or, conversely, whether they represent an early protective response is not yet known.

Human trophoblasts exposed to COVID-19 share antigenic responses and decreased collagen biosynthesis with MIA-exposed SpTs

To explore the potential translational relevance of our transcriptomic findings, we reanalyzed a single-cell RNA-sequencing dataset of placental tissue harvested from women with confirmed COVID-19 infections during pregnancy(*40*). That study reports inflammation within the placentas of COVID-19-infected women which was absent from healthy controls, and shows upregulation of granzymes *GZMA* and *GZMB*, consistent with our observation of the induction of granzymes in maternally derived immune cells following MIA (Fig. 3G). We next investigated the transcripts differentially expressed between COVID-19 and control conditions within villous cytotrophoblasts (VCTs) and extravillous trophoblasts (EVTs), two fetally-derived populations that are the human homologs of mouse SpTs(*41*). We identified subsets of genes upregulated in both COVID-19 and $\mathrm{poly(I{:}C)^{mod}}$ (spongio)trophoblasts, indicating that the placental response to viral infection in humans and mice partially converges. As expected, gene ontology (GO) analysis revealed that transcripts upregulated in $\mathrm{poly(I{:}C)^{mod}}$ SpTs (our data), COVID-19-exposed VCTs, and COVID-19 exposed EVTs share functions in neural tube development, placental morphogenesis, and *in utero* embryonic development (Fig. S7C). Conversely, genes upregulated in both SpTs and VCTs (but not EVTs) are associated with myeloid cell activation and hemopoiesis, consistent with our observation that SpTs express inflammatory factors following MIA. SpTs and EVTs (but not VCTs) upregulate genes associated with T cell activation and proliferation and leukocyte cell:cell adhesion, in line with our observation that responses of SpTs to MIA reflect not only innate immune processes but also adaptive immunity. Concurrently, both SpTs exposed to MIA and EVTs exposed to COVID-19 downregulate genes associated with connective tissue development and collagen biosynthesis and metabolism (Fig. S7C). Together, these findings suggest that MIA in both humans and mice promotes inflammatory responses in placental trophoblasts concurrent with a reduction in components of the extracellular matrix.

MIA disrupts the structural integrity of the decidua and junctional zone in poly(I:C)^{mod} and poly(I:C)^{strong} placentas

The dampening of ECM production and hormone signaling within placental cells suggests that MIA leads to a loss of structural integrity within the placenta. To test this hypothesis, we assessed placental architecture by scoring the severity of lesions revealed by H&E staining. We observed lesions that were restricted to the decidua and the junctional zone—characterized by classical pathological signs of hemorrhage, degeneration, congestion, and necrosis—in poly(I:C)$^{\text{mod}}$ and poly(I:C)$^{\text{strong}}$ placentas but not the placentas of male embryos that develop normally following MIA, or in the placentas of females from either treatment group (Fig. 4H-J and Fig. S8A-E). Given these striking sex-based differences, we also compared the architecture of untreated male and female placentas at E12.5, which indicated no lesions or other architectural differences between male and female placentas at baseline (Fig. S8F). Thus, a combination of bulk and single-cell transcriptomics, ECM immunostaining, and anatomical analyses reveal a male-specific breakdown in placental integrity downstream of MIA, particularly at the junctional zone, where maternal-fetal placental compartments meet. We further show that these disruptions only occur in the placentas of embryos exhibiting developmental abnormalities downstream of MIA.

Innate and adaptive immune cells infiltrate the amniotic fluid following MIA

Each mouse embryo is contained in a unique amniotic sac, surrounded by amniotic fluid (AF), a liquid comprised of both fetally and maternally derived cells and molecules that undergo active exchange with the fetus. Given the structural deterioration of the junctional zone and the inflammatory responses of both maternally- and fetally-derived cells within poly(I:C)$^{\text{mod}}$ placentas, we hypothesized that MIA alters the immune landscape of the AF, thereby contributing to developmental dysfunction in the embryo. However, while inflammatory signatures within the placenta have been observed in MIA models(*18-20, 33*), the impact of MIA on the composition of the AF has not been systematically investigated.

To measure the abundance and activation states of major immune cell classes within the AF, we subjected AF of male embryos across phenotypes and treatment groups to multispectral flow cytometry. This powerful approach allowed us to map the immune cell compartment of the AF across siblings within the same litters, obtaining >10,000 live cells per sample across the major immune lineages (defining markers given in parentheses): NK cells (NK1.1$^+$/NKp46$^+$), monocytes/macrophages (CD11b$^+$), dendritic cells (CD11c$^+$MHC-II$^+$), T cells (CD3$^+$), and B cells (CD19$^+$; Fig. S9). In addition to assessing the abundance of immune cells, we also measured their activation states as detailed below.

Comparing AF composition between saline and poly(I:C)-treated male embryos across phenotypes revealed a significant expansion of several immune cell populations following MIA. For example, MIA induced a robust increase in the abundance of monocytes in the AF of poly(I:C)-exposed male embryos versus control males regardless of phenotype (Fig. 5A,B). Monocyte (including macrophage) activation as measured by CD45+,CD11b+, Ly6C+ co-expression trends toward higher levels in poly(I:C)$^{\text{norm}}$ and poly(I:C)$^{\text{mod}}$ embryos and is significantly higher in poly(I:C)$^{\text{strong}}$ embryos versus saline, suggesting that the increased number of activated macrophages in the AF contributes to adverse phenotypes in the offspring. uNK cells are also significantly more abundant in the AF of poly(I:C)$^{\text{mod}}$ embryos compared to saline, a trend that we observed for poly(I:C)$^{\text{norm}}$ and poly(I:C)$^{\text{strong}}$ embryos as well (Fig. 5A,C). These cells are derived from the maternal decidua, in line with our observation that uNK cell abundance within the placenta is decreased by MIA (Fig. 3B). Interestingly, dendritic cell numbers are decreased in the AF of poly(I:C)-exposed males compared to saline, again regardless of phenotypic severity (Fig. 5D). In terms of adaptive immunity, significant changes in the abundance of B cells were not identified, and numbers of B cells in the amniotic fluid are low in general across conditions (Fig. 5A). However, somewhat unexpectedly, MIA significantly increases numbers of T cells within the AF of poly(I:C)$^{\mathrm{mod}}$ and poly(I:C)$^{\mathrm{strong}}$ placentas but not poly(I:C)$^{\mathrm{norm}}$ placentas, suggesting that, while changes in the abundance of innate immune cells within the AF extend across male embryos of all phenotypes, T cells are only present in the AF of embryos that exhibit deficits (Fig. 5A,E). Remarkably, the increased number of T cells occurs within poly(I:C)$^{\mathrm{mod}}$ and poly(I:C)$^{\mathrm{strong}}$ samples but not normally developing males even when all phenotypes were present in the same litter (Fig. 5F). Together, these findings provide evidence that MIA drives an influx of both innate and adaptive immune cells into the AF of male embryos within a 24-hour timeframe, poising maternally derived inflammatory signals to derail fetal development.

MIA induces a pro-inflammatory environment within the AF of poly(I:C)^{mod} and poly(I:C)^{strong} embryos

The remodeling of the immune cell repertoire in the AF of poly(I:C)-exposed male embryos provides evidence that inflammatory factors initiated in the dam lead to robust changes not just in the placenta but also in the direct environment of the fetus. To further delineate the immunological changes elicited by MIA in the AF and to relate these changes to developmental susceptibility, we performed multiplexed ELISAs to assess the expression of 37 cytokines and related soluble factors in females and males of all conditions and phenotypes. While most cytokines are unaffected by MIA regardless of phenotype, 14 cytokines exhibit an MIA-induced increase in expression within the AF of male fetuses exhibiting developmental abnormalities (i.e. poly(I:C)$^{\mathrm{strong}}$ and/or poly(I:C)$^{\mathrm{mod}}$ embryos) but not in normally developing males (poly(I:C)$^{\mathrm{norm}}$ mice; Fig. 5G). Strikingly, these 14 cytokines also fail to be significantly induced by poly(I:C) in the AF of female embryos (Table S1), suggesting a link to the developmental deficits observed in poly(I:C)$^{\mathrm{strong}}$ and/or poly(I:C)$^{\mathrm{mod}}$ males.

Cytokines induced by MIA in the AF of affected male embryos include the pro-inflammatory factors TNFα, Gm-CSF, MIP-2, IL-1β, IL-6, and IL-17. Both IL-6 and IL-17 have been previously associated with behavioral impairments in offspring of poly(I:C)-treated mice(*15, 17, 42-44*). In addition to this cohort of classical pro-inflammatory cytokines, several other Interleukin family members are induced by MIA in the AF of poly(I:C)$^{\mathrm{mod}}$ but not poly(I:C)$^{\mathrm{norm}}$ embryos: IL-2, -3, -5, and -11. As interleukins play a key role in mediating T and B cell activation, their selective presence within the AF of poly(I:C)$^{\mathrm{mod}}$ embryos further supports the idea that a transition from innate to adaptive immunity occurs in the direct environment of those fetuses (although at this early timepoint the innate immune response predominates), mirroring the responses observed in maternally-derived immune cells. Finally, LIF, KC, MCP-1, and IP-10, all of which are involved in immune cell chemotaxis and activation, also exhibit selective induction in poly(I:C)$^{\mathrm{mod}}$ versus poly(I:C)$^{\mathrm{norm}}$ embryos. Notably, increased levels of several of these cytokines (e.g. TNFα, IL-6, IL-17, IL-1β, and MCP-1) have been observed in the blood of mothers to children with ASD and the brains, cerebrospinal fluid, and blood of individuals with ASD, supporting the relevance of our findings to ASD in humans(*45-51*). Altogether, our analysis of the immune compartment of the AF revealed changes in cellular abundance and activation states that occur following MIA in all male embryos regardless of phenotype (with the exception of T cells which were absent from poly(I:C)^{norm} embryos), and changes in cytokine abundance that are selective to male embryos that are deleteriously affected by MIA. Similarly, female embryos do not exhibit an increase in cytokines within the AF following MIA (Table S1), suggesting that these cytokines contribute to the developmental deficits observed only in male embryos.

IL-6 is required for MIA-driven deficits in male fetal development

While our data identify multiple MIA-induced cytokines within the AF, IL-6 is among the most highly induced in poly(I:C)^{mod} and poly(I:C)^{strong}, but not poly(I:C)^{norm} or female, placentas (Fig. 6A,B). Moreover, IL-6 has been shown to promote ASD-like behavioral phenotypes of MIA$_{poly(I:C)}$ offspring(*17, 43*). Thus, we hypothesized that IL-6 links the early developmental deficits that we describe here to the ASD-like behavioral impairments previously characterized in adult offspring of MIA$_{poly(I:C)}$ mice.

To test this hypothesis, we used the MIA$_{poly(I:C)}$ paradigm but included neutralization of maternal IL-6 via intraperitoneal injection of the IL-6 neutralizing antibody MP5-30 one hour prior to exposure to poly(I:C). We validated depletion of IL-6 by ELISA of maternal blood as well as the AF (Fig. 6C,D). We find that, while poly(I:C) still elicits developmental abnormalities in about 30% of embryos at E13.5, it does not affect fetal health when IL-6 is neutralized (Fig. 6E-I). Thus, maternal IL-6 is not only necessary for the appearance of ASD-like behaviors in adult offspring following MIA, it is also necessary for the abnormalities in fetal development that emerge within 24 hours of poly(I:C) exposure. This finding suggests that IL-6 links inflammation at the maternal-fetal interface to the behavioral deficits that emerge in male fetuses following exposure to MIA.

Discussion:

While the vast majority of mechanistic studies on the biological drivers of ASD focus on the brain, the strong association between MIA and ASD risk indicates that prenatal immunological dysfunction is a critical, but understudied, contributor to disease etiology. By characterizing changes in fetal health that occur within 24 hours of poly(I:C) exposure, we identify male-specific developmental abnormalities that emerge following MIA. This result is consistent with published evidence that male offspring of MIA$_{poly(I:C)}$ mice exhibit more extreme behavioral and cognitive symptoms than females(*52, 53*), as well as emerging evidence that males exhibit heterogeneity in their behavioral responses to MIA(*29, 30, 54-56*). Our data suggest that, in cases where inflammation is involved, male bias in ASD arises in gestation rather than or in addition to accumulating over postnatal development.

At the mechanistic level, our analyses identify the placenta—particularly fetally derived SpTs at the junctional zone—as a primary target of MIA. snRNAseq and histological analyses reveal three convergent effects of maternal inflammation: (1) induction of immune and antigen-response programs across maternal and fetal placental cell types; (2) suppression of extracellular matrix and endocrine pathways, which are essential for maintaining an immunosuppressive placental microenvironment, in SpTs; and (3) structural degradation of the junctional zone, coinciding with immune cell and cytokine infiltration into the AF. Finally, we show that IL-6 infiltrates the AF and is required for the developmental deficits observed in male embryos exposed to MIA, consistent with IL-6 being necessary for the adult offspring of MIA mice to exhibit cognitive and behavioral deficits in the MIA$_{poly(I:C)}$ model(*43*). Thus, our work demonstrates that MIA induces a switch from an immunosuppressive placental microenvironment toward an inflammatory state characterized by the expression of factors that regulate the host immune response to non-self triggers (Fig. S10).

Based on these results, we hypothesize that two factors are necessary to give rise to developmental abnormalities following MIA: (1) an abundance of non-self proteins, i.e. antigens, derived from the fetus, and (2) an inflammatory placental microenvironment. In a healthy pregnancy, although male fetuses express high levels of paternally derived proteins, the placental microenvironment suppresses inflammation to protect and support the embryo. However, in the context of MIA, the placental microenvironment loses its immunosuppressive properties, allowing these fetally-derived antigens to activate maternal immune cells which ultimately injures the placenta and compromises fetal health. Although the placentas of female embryos exposed to poly(I:C) are also likely to lose some immunosuppressive properties as they are exposed to the same maternal factors, the lower burden of paternally derived antigens allows the placenta to maintain healthy development of the female fetus.

Our results are consistent with an immunological basis of some cases of ASD. In line with this interpretation, individuals with autoimmune disorders are more likely to have offspring diagnosed with ASD (*57-60*). Likewise, the increased abundance of pro-inflammatory cytokines within the blood of mothers to children with ASD and the brains, cerebrospinal fluid, and blood of individuals with ASD point toward a chronic inflammatory component to the pathophysiology of the disorder in a subset of patients, particularly in males. Notably, these cytokines include TNFα, IL-6, IL-17, and IL-1 (*46-51, 61, 62*) which were also identified in our data. IL-6 may be of particular relevance therapeutically as our data indicate that IL-6 is required for the emergence of MIA-driven developmental deficits, while work from other labs suggests that IL-6 is also necessary (and sufficient) to promote ASD-like behaviors in adult offspring exposed to MIA (*42, 43*).

Other evidence in humans points toward a potential role for maternal-fetal antigenicity in MIA-driven neurodevelopmental dysfunction as well. For example, maternal antibodies against fetal brain proteins were observed in about 12% of parents of children with ASD, and higher levels of these antibodies were positively correlated with the severity of neurodevelopmental impairments in autistic offspring(*63-67*). Moreover, ASD is more common in first-born children, potentially because this pregnancy is the first introduction of the maternal immune system to the fetus's antigens(*68*). ASD is also more common in children born to an older father(*68, 69*). This is relevant because advanced paternal age is associated with increased mutations in the sperm(*70, 71*), which could create new fetal antigens against which the maternal immune system may mount a response. Finally, although the question of whether maternal-fetal antigenicity contributes to male bias in ASD by rendering males more susceptible to maternal-fetal immune conflict remains unresolved, this immune incompatibility is already thought to contribute to other embryonic problems such as pre-eclampsia and intrauterine demise(*72*). Of note, our poly(I:C)^{strong} cohort appears to be in the process of intrauterine demise within 24 hours of MIA, consistent with this association. These observations suggest that some cases of ASD may share pathophysiological mechanisms, but have less extreme outcomes, with conditions like pre-eclampsia.

Limitations of the study:

This study has several limitations. The use of a mouse model limits direct extrapolation to human pregnancy, and aspects of placental architecture and immune regulation differ between the species. Experiments expanded to crosses between unrelated (i.e. not inbred) mouse strains could be an informative future direction, as these would be more likely to unveil antigenicity between mother and fetus given their distinctive genetic backgrounds. Another caveat that is important to consider is the high degree of variability that hampers MIA models, wherein factors as basic as the commercial source of the poly(I:C) can dramatically change the impact of MIA on fetal neurodevelopment(*25-27*). Finally, our focus on early embryonic outcomes precluded direct assessment of how cytokines in the AF influence fetal brain development. Despite these caveats, our findings define early determinants of susceptibility versus resilience to prenatal inflammation and highlight the maternal–fetal interface as a critical site of ASD risk.

STAR Methods:

Animal models

All experiments were performed in compliance with protocols approved by the Institutional Animal Care and Use Committee (IACUC) at Cold Spring Harbor Laboratory. The following mouse lines were used in the study: C57Bl/6J (The Jackson Laboratory, JAX:000664) and BALB/cJ (JAX:000651). Mice were maintained in standard housing at 20–22°C with 40–55% humidity on a 12-hour light/dark cycle, with food and water provided ad libitum.

Maternal Immune Activation (MIA)

C57BL/6J or BALB/c mice maintained in-house for ≥3 generations were used for breeding unless otherwise indicated. Estrous cycle stage was determined via daily vaginal lavage, and females in proestrus were housed overnight with proven males. The visible presence of sperm or a vaginal plug the following morning marked embryonic day E0.5, and the male was removed at this time. MIA was induced at E12.5 (with smaller cohorts being induced at E9.5 or E14.5) by intraperitoneal injection of polyinosinic–polycytidylic acid [poly(I:C), 20 mg/kg; Sigma-Aldrich P9582] or sterile saline as a control. Dams were euthanized 24 hours post-treatment (E13.5 for most experiments) and embryos, placentas, and amniotic fluid were collected.

Validation of MIA

Maternal blood was collected immediately before poly(I:C) injection at 0 hours and 3 hours post-injection via facial or submandibular vein puncture using a sterile 5 mm lancet (Goldenrod Animal Lancet). Approximately 200 µL of whole blood was collected per time point, centrifuged at 1,400 × g for 10 minutes at 4°C, and ≥25 µL of serum was transferred to Protein LoBind microtubes and stored at 4°C for up to 24 hours. Maternal IL-6 concentrations were quantified using a commercial ELISA (R&D Systems DY406-05). Absorbance at 450 nm was measured, and concentrations were calculated by four-parameter logistic fitting. Dams that failed to mount a sufficient IL-6 response or exhibited severe illness/spontaneous abortion were excluded from further analyses.

Quantification of developmental abnormalities in embryos

Embryos were imaged under a stereomicroscope Nikon SMZ1500, and morphological measurements were obtained using ImageJ. In addition to fetal weight, parameters measured include crown–rump length (CRL), anterior–posterior diameter (APD), hind limb length, lambda–bregma distance, mandibular plane length, and muzzle–auricular angle. In addition, the percentage of the surface of each embryo displaying vascular hemorrhaging was quantified. Additional categorical scoring captured abnormalities in the ears, whisker pad, tail, and spine. Measurements were summarized at the litter level to assess within-litter penetrance.

MCA Analysis

Morphological traits were binarized and analyzed by Multiple Correspondence Analysis (MCA) implemented in Python using prince, pandas, and matplotlib packages. Embryos were assigned to poly(I:C)^{norm}, poly(I:C)^{mod}, or poly(I:C)^{strong} categories based on predefined morphological criteria. Group ellipses were derived from covariance matrices and scaled to encompass approximately 95% of observations, representing dispersion rather than confidence intervals. Ellipses were centered at group centroids and aligned to the principal direction of variance. All visualizations were exported as vector-based PDF files for downstream editing.

Sex determination

Embryonic sex was determined by PCR genotyping of tail samples using primers for *Rbm31* which takes different forms when expressed on the X versus the Y chromosome. When the Y chromosome is present, a larger fragment is amplified, allowing us to confidently annotate embryos as male or female depending upon whether this band was present (males) or not (females). We further validated these sex assignments through PCR for the Y-chromosome-specific gene SRY. Primer sequences used were: *Rbm31* (forward), 5’-CACCTTAAGAACAAGCCAATACA-3’; *Rbm31* (reverse), 5’-GGCTTGTCCTGAAAACATTTGG-3’; *SRY* (forward), 5’-GGAGTGGCATTTTACAGCCTGC-3’; *SRY* (reverse), 5’-TGGAGTACAGGTGTGCAGCTCT-3’. PCR products were resolved by agarose gel electrophoresis.

Bulk RNA sequencing

Placentas were collected from saline-treated control males or poly(I:C)^{mod} males under a Nikon SMZ1500 stereomicroscope and weighed. About 20 mg of placental tissue was then subjected to RNA extraction. Tissue was transferred to QIAGEN Buffer RLT supplemented with β-mercaptoethanol used to enhance RNase inactivation. and homogenized with ceramic beads using a BeadBug™ 6 microtube homogenizer (Benchmark Scientific) until no visible fragments remained. Total RNA was purified using the RNeasy Mini Kit (QIAGEN, cat. no. 74106) according to the manufacturer’s instructions, including on-column DNase digestion using the RNase-Free DNase Set (QIAGEN; Buffer RDD). Purified RNA was eluted in RNase-free water and stored at −80°C until library preparation and sequencing. Libraries were sequenced on an Illumina NextSeq 2000 using paired-end 150-bp reads (300-cycle configuration), yielding ~400 million reads in total across all samples.

Paired-end FASTQ files were initially assessed for sequencing quality using FastQC (Babraham Bioinformatics). Adapter trimming and quality filtering were performed using fastp in paired-end mode with a Q20 quality threshold and overrepresentation analysis enabled, followed by post-trimming quality assessment using FastQC. High-quality reads were aligned to the mouse reference genome (mm10) using the splice-aware aligner STAR. The STAR genome index was generated from the mm10 genome FASTA and corresponding gene annotation GTF obtained from a publicly available reference package (refdata-gex-mm10-2020-A). Alignments were performed with multithreading and on-the-fly decompression of gzipped FASTQ files, and outputs were generated as coordinate-sorted BAM files. Gene-level read counts were quantified from sorted BAM files using HTSeq-count, counting reads overlapping annotated exons and summarizing counts at the Ensembl gene_id level in unstranded mode.

Differential gene expression analysis was conducted in R (v4.4.3) using DESeq2. Raw gene count matrices were combined across samples and aligned with sample metadata, and differential expression was modeled using negative binomial generalized linear models with experimental condition specified as the primary explanatory variable. Resulting *P* values were adjusted for multiple hypothesis testing using the Benjamini–Hochberg false discovery rate correction. Gene identifiers were annotated by mapping Ensembl gene IDs to official gene symbols using biomaRt with the Ensembl *Mus musculus* database. For visualization, size-factor–normalized counts were $\log_2$-transformed after adding a pseudocount of 1, and expression levels of selected genes were visualized using boxplots overlaid with individual sample points; statistical significance was annotated directly from adjusted *P* values (without re-testing). Data manipulation and visualization were performed using dplyr, tidyr, and ggplot2. Functional enrichment analyses were carried out using clusterProfiler, with curated gene sets obtained from msigdbr and enrichment testing performed using fgsea, as indicated. Heatmaps were generated using ComplexHeatmap or pheatmap, as specified.

Single-nucleus RNA sequencing (snRNAseq)

Tissue preparation

For snRNAseq, placentas from saline-exposed and poly(I:C)^{mod} male embryos were flash-frozen in liquid nitrogen. Frozen tissues were thawed in 1 ml of high sucrose buffer containing 0.25 M sucrose, 25 mM KCl, 5 mM $MgCl_2$, 20 mM Tricine-KOH, pH 7.8, 0.15 mM spermine tetrahydrochloride, 0.5 mM spermidine trihydrochloride, 1 mM DTT in the presence of RNAse inhibitors. The samples were mechanically dissociated using a Dounce homogenizer containing IGEPAL CA-630 (Sigma-Aldrich). Nuclei were collected from the interface of 30% and 40% of iodixanol after 18 minutes of density gradient ultracentrifugation at 10,000 x g. Purified nuclei were counted using a hemocytometer and processed as per the 10x Chromium Next GEM Single Cell 3’ v3.1 kit to recover approximately 10,000 nuclei/ml. Libraries were sequenced at The Center for Applied Genomics (TCAG), The Hospital for Sick Children, Toronto, ON, Canada.

Bioinformatics workflow

snRNAseq data processing and downstream analyses were performed using the Cell Ranger and Seurat pipelines. Raw sequencing reads were demultiplexed and aligned to the mouse reference genome (mm10) using Cell Ranger (10x Genomics, v7.1.0), generating gene-by-nucleus count matrices for each library. Ambient RNA contamination, a common artifact of droplet-based sequencing platforms, was corrected using SoupX (v1.6.2), which automatically estimates and removes background RNA signatures originating from empty droplets. This correction improved cluster separation and biological signal clarity in subsequent analyses.

Following data import, nuclei with fewer than 200 or more than 2,500 detected genes, as well as those with greater than 5% mitochondrial gene content, were excluded to remove low-quality nuclei and potential doublets. Data normalization and variance stabilization were performed using Seurat’s SCTransform function to enable accurate scaling and gene expression comparisons across samples. For integrated analyses across biological replicates and experimental conditions, datasets were merged using the Seurat integration pipeline (v5.0.1) in conjunction with Harmony batch correction (v0.1.1), which mitigates technical variability while preserving biologically meaningful differences.

Dimensionality reduction was performed using principal component analysis (PCA), with the top 30 principal components retained for downstream analyses. A shared nearest-neighbor (SNN) graph was constructed based on these components to capture transcriptomic relationships among nuclei. Clustering was performed using the Louvain algorithm (resolution = 0.8), and low-dimensional visualization was generated using Uniform Manifold Approximation and Projection (UMAP) with 30 dimensions. Cluster identities were assigned based on the expression of canonical lineage-specific marker genes.

Differential gene expression (DGE) analysis

Differential gene expression analyses were performed for each identified cell type using the Model-based Analysis of Single-cell Transcriptomics (MAST) framework, implemented through Seurat’s FindMarkers function. Biological replicates were included as a latent variable to account for inter-sample variability within each experimental group, ensuring robust identification of consistent transcriptional changes. To restrict analyses to reliably expressed genes, only genes detected in at least 5% of nuclei in either condition were tested. Differentially expressed genes (DEGs) were defined by an FDR-adjusted p-value < 0.05 and an absolute $\log_2$ fold change ≥ 4.

Gene Ontology (GO) Enrichment Analysis

Functional enrichment analysis was performed on significantly differentially expressed genes using the clusterProfiler package (v4.0). Gene sets included DEGs with FDR-adjusted p-values < 0.05 and $\log_2$ fold changes ≥ 4 (upregulated) or ≤ -4 (downregulated). Gene Ontology (GO) terms containing fewer than 10 or more than 500 genes were excluded to avoid overly narrow or broadly defined categories. Multiple hypothesis testing was corrected using the Benjamini–Hochberg method, and GO terms were considered significantly enriched if they met both an FDR < 0.05 and a gene ratio > 0.1. Upregulated and downregulated gene sets were analyzed independently to identify condition-specific biological pathways.

Single-molecule fluorescence in situ hybridization (smFISH)

Coronal sections (12 µm) of placenta were generated using a Leica CM3050S cryostat, collected on Superfrost Plus slides, and stored at −80 °C until use. Multiplexed smFISH was performed using the RNAscope platform (Advanced Cell Diagnostics [ACD], Biotechne) following the manufacturer’s instructions for fresh-frozen samples (kit v2). Probes targeting *Ascl2 (Mash2)* and *Psg23* transcripts were used. For imaging, 40X confocal images were acquired as 5×5 tile scans using an LSM 780 Zeiss microscope. Three mice per condition were analyzed, with two images collected per mouse.

To quantify the proportion of cells positive for *Ascl2* and *Psg23*, images were processed as follows. First, the DAPI channel was thresholded and binarized, then expanded using the dilate function. The expanded DAPI mask was subjected to a watershed filter to ensure separation of adjacent nuclei. This mask was used to generate cell-specific regions of interest (ROIs), each corresponding to a single cell. For each ROI, the mean gray value within the *Ascl2* and *Psg23* channels was measured. The resulting values were exported into Excel for intensity-based classification. Background intensity for each marker was manually defined, and ROIs with mean intensities above background were assigned a value of 1 (positive), whereas ROIs below background were assigned a value of 0 (negative). These binarized datasets were used to calculate the percentage of cells positive for each transcript and the proportion of cells co-expressing *Ascl2* and *Psg23*.

Human scRNA-seq Re-analysis

The GSE171381 dataset represents single-cell RNA sequencing of placental tissue from mothers infected with COVID-19 during pregnancy. Raw count matrices and metadata from GSE171381 were imported into Seurat(v5). Ambient RNA contamination was removed using decontX (celda). Decontaminated counts were normalized and processed using standard Seurat workflows. Single-cell clustering was performed according to the original published cell-type annotations ("annotation_merged"). Differentially expressed genes between COVID-19 and control samples were identified within each cell type using Seurat's Wilcoxon test and MAST. Only genes exceeding a $\log_2$ fold change ≥ 2 with a p-value ≤ 0.05 were considered. Significant DEGs from human villous cytotrophoblasts (VCT), extravillous trophoblasts (EVT), and mouse spongiotrophoblasts (Spt) were compiled. Gene symbol formatting was standardized, and overlapping sets were quantified in Excel. GO enrichment analysis was performed on overlapping DEGs using clusterProfiler. Analyses included biological process (BP), cellular component (CC), and molecular function (MF) ontologies, and the top-enriched terms were visualized using standard plotting functions within the package.

Placental pathology

Mouse placentas were harvested and immediately immersion-fixed in ice-cold 4% paraformaldehyde (PFA) in PBS overnight at 4°C. After fixation, tissues were transferred to 70% ethanol and processed for paraffin embedding. Paraffin sections were stained with hematoxylin and eosin (H&E) and cut parallel to the chorionic plate and evaluated by a placental pathologist blinded to condition. Degeneration, vascular congestion, trophoblast degeneration, and necrosis were scored on a 0–5 scale. Representative images were acquired under identical imaging settings. Scores were compared across groups by one-way ANOVA followed by Tukey's post hoc correction, or two-way ANOVA where appropriate.

Immunofluorescence

Placentas were harvested and immediately immersion-fixed in ice-cold 4% paraformaldehyde (PFA) in PBS overnight at 4°C. Following fixation, tissues were cryoprotected by incubation in 15% sucrose and then 30% sucrose (in PBS) until fully infiltrated, embedded in OCT (stored at −80°C), and sectioned into transverse sections perpendicular to the chorionic plate at 12 µm onto Superfrost Plus slides using a Leica CM3050 S cryostat. Sections were washed in PBS and blocked in blocking solution (PBS containing 5% normal goat serum [NGS] and 0.3% Triton X-100 [TX-100]) for 1 hour at room temperature, then incubated overnight at 4°C in primary antibody (Rabbit anti-Col1a1, Cell Signaling Technologies 72026S, [1:300]) diluted in blocking solution . The next day, sections were washed 3 times for 10 minutes per wash in PBS before incubation in secondary antibody Alexafluor 555 rabbit anti-goat (Thermofisher A21428; [1:1000]) diluted in probing solution (PBS with 5% normal goat serum and 0.3% Triton X-100) for 2 hours at room temperature. Sections were then washed in PBS, stained for 10 minutes with

NucBlue™ (Invitrogen,R37605) mounted in fluoromount-G (SouthernBiotech), and cover-slipped.

Col1a1 fluorescence was imaged on a Zeiss LSM 710 confocal microscope as Z-stacks using identical acquisition settings across groups and converted to maximum intensity projections in Fiji/ImageJ. Images were processed identically across samples, including rolling-ball background subtraction applied uniformly. Anatomically matched ROIs were defined with comparable quantified tissue area across samples, and Col1a1 signal was quantified as mean fluorescence intensity (mean gray value) within each ROI, excluding saturated pixels and tissue artifacts. Multiple ROIs/sections were averaged per biological replicate and exported for downstream statistical analysis.

Flow cytometric analysis of amniotic fluid

Amniotic fluid was collected from individual embryos into pre-chilled low-bind microtubes and kept on ice. Samples were diluted in cold FACS buffer (PBS + 2% FBS) and passed through a 40–70 µm cell strainer to remove debris and aggregates. Cells were pelleted by centrifugation at 500 × g for 7 min at 4°C. Supernatants were removed and retained for cytokine measurements when indicated, and cell pellets were gently resuspended in FACS buffer. Cells were incubated with anti-mouse CD16/32 (Fc receptor-blocking antibody; BioLegend, clone 2.4G2) to prevent non-specific antibody binding for 10 min at 4°C, followed by staining with a fixable viability dye and surface antibody cocktails (panel in supplementary material S9-A) for 25–30 min at 4°C in the dark. Samples were washed twice with FACS buffer and resuspended in FACS buffer for acquisition.

Single color reference controls were prepared using both cells and antibody capture beads, together with an unstained control, and acquired in parallel. Data were acquired on a Sony ID7000 spectral flow cytometer, and spectral unmixing, including autofluorescence extraction when applicable, was performed using the reference controls. Gating strategies were standardized across samples to define major immune lineages: monocytes/macrophages, NK cells, dendritic cells, and T cells. Dimensionality reduction was performed using viSNE on the Cytobank platform.

Amniotic fluid cytokine evaluation

Cytokines and chemokines were quantified from 20–30 µL of embryo-specific amniotic fluid using a 32-plex bead-based immunoassay (Luminex® xMAP®; MILLIPLEX® Mouse Cytokine/Chemokine 32-Plex, MCYTOMAG-70K), performed by Eve Technologies (Calgary, AB, Canada) on a Luminex® 200™ system. The panel measured inflammatory cytokines (e.g., TNF-α, IL-1α/β, IL-6, IL-10, IFN-γ), T-cell–associated cytokines (e.g., IL-2, IL-4, IL-5, IL-7, IL-9, IL-12p40/p70, IL-13, IL-15, IL-17), growth factors (e.g., G-CSF, GM-CSF, M-CSF, VEGF-A), and chemokines (e.g., CCL2/MCP-1, CCL3/MIP-1α, CCL4/MIP-1β, CCL5/RANTES, CCL11/Eotaxin, CXCL1/KC, CXCL2/MIP-2, CXCL9/MIG, CXCL10/IP-10, LIX). Concentrations were exported as CSV and processed in Python, non-numeric outputs were treated as missing and imputed using the cytokine-specific median. To harmonize analyte dynamic ranges, each cytokine was transformed using a robust Z-score; values were clipped to ±7.5 for visualization only. Heatmaps were generated per embryo (no litter averaging) and exported as vector PDFs.

IL-6 blockade during MIA

Pregnant dams were assigned to saline, poly(I:C), or poly(I:C) + IL-6 blockade groups. For IL-6 blockade, dams received anti–mouse IL-6 (clone MP5-30) at 8.3 mg/kg (166 µg for a 20 g dam; i.p.) 1 hour prior to poly(I:C) administration. Maternal serum and amniotic fluid were collected for IL-6 quantification as described above. Embryos were assessed for developmental abnormalities using standardized craniofacial and axial morphological metrics. Group differences were analyzed by one-way ANOVA with post hoc multiple-comparison testing, and representative images were acquired under identical settings.

Statistical analyses

For all analyses, sample sizes were chosen based on previously generated data and/or power analyses. Acquired data was first tested for normality and log-normality before choosing a parametric or non-parametric statistical test. When the data were found to be normally distributed, parametric t-tests, one-way ANOVAs, or repeated measures two-way ANOVAs were used. If data were found to be non-Gaussian and non-logarithmic, a Mann-Whitney test was performed.

Statistical analyses were performed in Excel and Prism 9.0 (GraphPad Software). Figures were created using Python and Graphpad Prism and formatted using Adobe Illustrator (2024). The models were generated in biorender.com. Data are presented as mean ± SEM unless otherwise indicated.

References and Notes:

1. C. A. Boyle *et al.*, Trends in the prevalence of developmental disabilities in US children, 1997-2008. *Pediatrics* **127**, 1034–1042 (2011).
2. M. D. Kogan *et al.*, The Prevalence of Parent-Reported Autism Spectrum Disorder Among US Children. *Pediatrics* **142**, (2018).
3. G. Xu *et al.*, Prevalence and Treatment Patterns of Autism Spectrum Disorder in the United States, 2016. *JAMA Pediatr* **173**, 153–159 (2019).
4. J. A. S. Vorstman *et al.*, Autism genetics: opportunities and challenges for clinical translation. *Nat Rev Genet* **18**, 362–376 (2017).
5. A. G. Edlow, V. M. Castro, L. L. Shook, A. J. Kaimal, R. H. Perlis, Neurodevelopmental Outcomes at 1 Year in Infants of Mothers Who Tested Positive for SARS-CoV-2 During Pregnancy. *JAMA Netw Open* **5**, e2215787 (2022).
6. S. Chess, Autism in children with congenital rubella. *J Autism Child Schizophr* **1**, 33–47 (1971).
7. A. S. Brown *et al.*, A.E. Bennett Research Award. Prenatal rubella, premorbid abnormalities, and adult schizophrenia. *Biol Psychiatry* **49**, 473–486 (2001).
8. B. K. Lee *et al.*, Maternal hospitalization with infection during pregnancy and risk of autism spectrum disorders. *Brain Behav Immun* **44**, 100–105 (2015).

9. D. L. Christensen *et al.*, Prevalence and Characteristics of Autism Spectrum Disorder Among Children Aged 8 Years - Autism and Developmental Disabilities Monitoring Network, 11 Sites, United States, 2012. *MMWR Surveill Summ* **65**, 1–23 (2018).
10. K. J. Baines, R. C. West, Sex differences in innate and adaptive immunity impact fetal, placental, and maternal healthdagger. *Biol Reprod* **109**, 256–270 (2023).
11. J. G. Eriksson, E. Kajantie, C. Osmond, K. Thornburg, D. J. Barker, Boys live dangerously in the womb. *Am J Hum Biol* **22**, 330–335 (2010).
12. E. Kim, J. R. Huh, G. B. Choi, Prenatal and postnatal neuroimmune interactions in neurodevelopmental disorders. *Nat Immunol* **25**, 598–606 (2024).
13. N. V. Malkova, C. Z. Yu, E. Y. Hsiao, M. J. Moore, P. H. Patterson, Maternal immune activation yields offspring displaying mouse versions of the three core symptoms of autism. *Brain Behav Immun* **26**, 607–616 (2012).
14. L. Zuckerman, I. Weiner, Maternal immune activation leads to behavioral and pharmacological changes in the adult offspring. *J Psychiatr Res* **39**, 311–323 (2005).
15. M. D. Reed *et al.*, IL-17a promotes sociability in mouse models of neurodevelopmental disorders. *Nature* **577**, 249–253 (2020).
16. Y. Shin Yim *et al.*, Reversing behavioural abnormalities in mice exposed to maternal inflammation. *Nature* **549**, 482–487 (2017).
17. E. Y. Hsiao, P. H. Patterson, Activation of the maternal immune system induces endocrine changes in the placenta via IL-6. *Brain Behav Immun* **25**, 604–615 (2011).
18. C. Shen *et al.*, The rebalancing of the immune system at the maternal-fetal interface ameliorates autism-like behavior in adult offspring. *Cell Rep* **43**, 114787 (2024).
19. J. Kwon, M. Suessmilch, A. McColl, J. Cavanagh, B. J. Morris, Distinct trans-placental effects of maternal immune activation by TLR3 and TLR7 agonists: implications for schizophrenia risk. *Sci Rep* **11**, 23841 (2021).
20. H. C. Osman *et al.*, Impact of maternal immune activation and sex on placental and fetal brain cytokine and gene expression profiles in a preclinical model of neurodevelopmental disorders. *J Neuroinflammation* **21**, 118 (2024).
21. S. Marshall-Clarke *et al.*, Polyinosinic acid is a ligand for toll-like receptor 3. *J Biol Chem* **282**, 24759–24766 (2007).
22. C. S. Lim *et al.*, TLR3 forms a highly organized cluster when bound to a poly(I:C) RNA ligand. *Nat Commun* **13**, 6876 (2022).
23. H. O. Atladottir *et al.*, Association of hospitalization for infection in childhood with diagnosis of autism spectrum disorders: a Danish cohort study. *Arch Pediatr Adolesc Med* **164**, 470–477 (2010).
24. M. B. Hall, D. E. Willis, E. L. Rodriguez, J. M. Schwarz, Maternal immune activation as an epidemiological risk factor for neurodevelopmental disorders: Considerations of timing, severity, individual differences, and sex in human and rodent studies. *Front Neurosci* **17**, 1135559 (2023).
25. K. E. Tillmann *et al.*, Differential effects of purified low molecular weight Poly(I:C) in the maternal immune activation model depend on the laboratory environment. *Transl Psychiatry* **14**, 300 (2024).
26. F. S. Mueller *et al.*, Influence of poly(I:C) variability on thermoregulation, immune responses and pregnancy outcomes in mouse models of maternal immune activation. *Brain Behav Immun* **80**, 406–418 (2019).
27. H. M. Kowash *et al.*, Poly(I:C) source, molecular weight and endotoxin contamination affect dam and prenatal outcomes, implications for models of maternal immune activation. *Brain Behav Immun* **82**, 160–166 (2019).

28. J. J. Schwartzer *et al.*, Maternal immune activation and strain specific interactions in the development of autism-like behaviors in mice. *Transl Psychiatry* **3**, e240 (2013).
29. R. Schaer, F. S. Mueller, T. Notter, U. Weber-Stadlbauer, U. Meyer, Intrauterine position effects in a mouse model of maternal immune activation. *Brain Behav Immun* **120**, 391–402 (2024).
30. U. Meyer *et al.*, The time of prenatal immune challenge determines the specificity of inflammation-mediated brain and behavioral pathology. *J Neurosci* **26**, 4752–4762 (2006).
31. X. Jiang *et al.*, A differentiation roadmap of murine placentation at single-cell resolution. *Cell Discov* **9**, 30 (2023).
32. B. Marsh, R. Blelloch, Single nuclei RNA-seq of mouse placental labyrinth development. *Elife* **9**, (2020).
33. Q. Bian *et al.*, Maternal natural killer cells drive neuroimmune disorders in offspring through aberrant secretion of extracellular granzyme B. *Immunity* **58**, 1502–1518 e1508 (2025).
34. T. Napso, H. E. J. Yong, J. Lopez-Tello, A. N. Sferruzzi-Perri, The Role of Placental Hormones in Mediating Maternal Adaptations to Support Pregnancy and Lactation. *Front Physiol* **9**, 1091 (2018).
35. T. Tsukada *et al.*, Decidual cells are the initial target of polyriboinosinic-polyribocytidylic acid in a mouse model of maternal viral infection. *Biochem Biophys Rep* **26**, 100958 (2021).
36. F. F. Martinez, L. Cervi, C. P. Knubel, G. M. Panzetta-Dutari, C. C. Motran, The role of pregnancy-specific glycoprotein 1a (PSG1a) in regulating the innate and adaptive immune response. *Am J Reprod Immunol* **69**, 383–394 (2013).
37. T. Moore *et al.*, Pregnancy-specific glycoproteins: evolution, expression, functions and disease associations. *Reproduction* **163**, R11–R23 (2022).
38. S. K. Snyder *et al.*, Pregnancy-specific glycoproteins function as immunomodulators by inducing secretion of IL-10, IL-6 and TGF-beta1 by human monocytes. *Am J Reprod Immunol* **45**, 205–216 (2001).
39. L. Vicovac, M. Bozic, Z. Bojic-Trbojevic, S. Golubovic, Carcinoembryonic antigen and related molecules in normal and transformed trophoblast. *Placenta* **28**, 85–96 (2007).
40. A. Lu-Culligan *et al.*, Maternal respiratory SARS-CoV-2 infection in pregnancy is associated with a robust inflammatory response at the maternal-fetal interface. *Med* **2**, 591–610 e510 (2021).
41. M. Hemberger, C. W. Hanna, W. Dean, Mechanisms of early placental development in mouse and humans. *Nat Rev Genet* **21**, 27–43 (2020).
42. W. L. Wu, E. Y. Hsiao, Z. Yan, S. K. Mazmanian, P. H. Patterson, The placental interleukin-6 signaling controls fetal brain development and behavior. *Brain Behav Immun* **62**, 11–23 (2017).
43. S. E. Smith, J. Li, K. Garbett, K. Mirnics, P. H. Patterson, Maternal immune activation alters fetal brain development through interleukin-6. *J Neurosci* **27**, 10695–10702 (2007).
44. Y. Lee *et al.*, Brain-wide mapping of immune receptors uncovers a neuromodulatory role of IL-17E and the receptor IL-17RB. *Cell* **188**, 2203–2217 e2217 (2025).
45. M. W. Abdallah *et al.*, Amniotic fluid chemokines and autism spectrum disorders: an exploratory study utilizing a Danish Historic Birth Cohort. *Brain Behav Immun* **26**, 170–176 (2012).
46. S. Ricci *et al.*, Altered cytokine and BDNF levels in autism spectrum disorder. *Neurotox Res* **24**, 491–501 (2013).

47. C. A. Molloy *et al.*, Elevated cytokine levels in children with autism spectrum disorder. *J Neuroimmunol* **172**, 198–205 (2006).
48. P. Ashwood *et al.*, Associations of impaired behaviors with elevated plasma chemokines in autism spectrum disorders. *J Neuroimmunol* **232**, 196–199 (2011).
49. M. C. Inga Jacome *et al.*, Peripheral Inflammatory Markers Contributing to Comorbidities in Autism. *Behav Sci (Basel)* **6**, (2016).
50. C. C. Hu *et al.*, Alterations in plasma cytokine levels in chinese children with autism spectrum disorder. *Autism Res* **11**, 989–999 (2018).
51. D. L. Vargas, C. Nascimbene, C. Krishnan, A. W. Zimmerman, C. A. Pardo, Neuroglial activation and neuroinflammation in the brain of patients with autism. *Ann Neurol* **57**, 67–81 (2005).
52. S. Sal-Sarria, N. M. Conejo, H. Gonzalez-Pardo, Maternal immune activation and its multifaceted effects on learning and memory in rodent offspring: A systematic review. *Neurosci Biobehav Rev* **164**, 105844 (2024).
53. W. A. Carlezon, Jr. *et al.*, Maternal and early postnatal immune activation produce sex-specific effects on autism-like behaviors and neuroimmune function in mice. *Sci Rep* **9**, 16928 (2019).
54. U. Meyer, Neurodevelopmental Resilience and Susceptibility to Maternal Immune Activation. *Trends Neurosci* **42**, 793–806 (2019).
55. R. Schaer, N. Wenger, F. Herrero, T. Notter, U. Meyer, Ontogeny and plasticity of resilience and susceptibility in a mouse model of maternal immune activation. *Brain Behav Immun* **129**, 666–680 (2025).
56. F. Herrero *et al.*, Susceptibility and resilience to maternal immune activation are associated with differential expression of endogenous retroviral elements. *Brain Behav Immun* **107**, 201–214 (2023).
57. F. A. Yousef Yengej, A. van Royen-Kerkhof, R. Derksen, R. D. E. Fritsch-Stork, The development of offspring from mothers with systemic lupus erythematosus. A systematic review. *Autoimmun Rev* **16**, 701–711 (2017).
58. Z. Zhu, S. Tang, X. Deng, Y. Wang, Maternal Systemic Lupus Erythematosus, Rheumatoid Arthritis, and Risk for Autism Spectrum Disorders in Offspring: A Meta-analysis. *J Autism Dev Disord* **50**, 2852–2859 (2020).
59. A. Keil *et al.*, Parental autoimmune diseases associated with autism spectrum disorders in offspring. *Epidemiology* **21**, 805–808 (2010).
60. L. A. Needleman, A. K. McAllister, The major histocompatibility complex and autism spectrum disorder. *Dev Neurobiol* **72**, 1288–1301 (2012).
61. P. E. Goines *et al.*, Increased midgestational IFN-gamma, IL-4 and IL-5 in women bearing a child with autism: A case-control study. *Mol Autism* **2**, 13 (2011).
62. K. L. Jones *et al.*, Autism with intellectual disability is associated with increased levels of maternal cytokines and chemokines during gestation. *Mol Psychiatry* **22**, 273–279 (2017).
63. D. Braunschweig *et al.*, Autism-specific maternal autoantibodies recognize critical proteins in developing brain. *Transl Psychiatry* **3**, e277 (2013).
64. D. Braunschweig *et al.*, Autism: maternally derived antibodies specific for fetal brain proteins. *Neurotoxicology* **29**, 226–231 (2008).
65. P. Goines *et al.*, Autoantibodies to cerebellum in children with autism associate with behavior. *Brain Behav Immun* **25**, 514–523 (2011).
66. D. Braunschweig *et al.*, Behavioral correlates of maternal antibody status among children with autism. *J Autism Dev Disord* **42**, 1435–1445 (2012).

67. D. Braunschweig *et al.*, Maternal autism-associated IgG antibodies delay development and produce anxiety in a mouse gestational transfer model. *J Neuroimmunol* **252**, 56–65 (2012).
68. M. S. Durkin *et al.*, Advanced parental age and the risk of autism spectrum disorder. *Am J Epidemiol* **168**, 1268–1276 (2008).
69. S. Wu *et al.*, Advanced parental age and autism risk in children: a systematic review and meta-analysis. *Acta Psychiatr Scand* **135**, 29–41 (2017).
70. M. D. C. Neville *et al.*, Sperm sequencing reveals extensive positive selection in the male germline. *Nature* **647**, 421–428 (2025).
71. V. Seplyarskiy *et al.*, Hotspots of human mutation point to clonal expansions in spermatogonia. *Nature* **647**, 429–435 (2025).
72. A. Y. Collier, L. A. Smith, S. A. Karumanchi, Review of the immune mechanisms of preeclampsia and the potential of immune modulating therapy. *Hum Immunol* **82**, 362–370 (2021).

Acknowledgments:

We thank Dr. Michael Wigler for insightful input at an early stage in the project. We also thank the following individuals for critical input and feedback on the manuscript: Dr. Corina Amor Vegas (CSHL), Dr. Jeremy Borniger (CSHL), Dr. Patrick Mitchell (University of Washington), Dr. Marty Yang (University of California in Los Angeles), Dr. Austin Ferro (CSHL), and Dr. Dominic Vita (CSHL). We also thank Life Science Editors for assistance with editing the final draft. We acknowledge the CSHL Cancer Center Microscopy Shared Resources for services and technical expertise (NCI 2P30CA045508). We also acknowledge the flow cytometry core facility and the histology core at CSHL.

Funding:

National Institutes of Health grant R00MH120051 (LC)

National Institutes of Health grant DP2MH132943 (LC)

NIH Cancer Center support grant 5P30CA045508-36 (LC)

Rita Allen Foundation (LC)

McKnight Foundation (LC)

Klingenstein-Simons Fellowship Award in Neuroscience (LC)

Brain and Behavior Research Foundation (LC)

Author contributions:

Conceptualization: LC, ISM

Methodology: LC, ISM, BTK

Formal Analysis: PH

Investigation: ISM, BK, PH, QL, DD, VB, JP

Writing – original draft: LC

Writing – review & editing: LC, BTK, ISM

Visualization: LC, ISM, BK, PH, QL

Supervision: LC, BTK

Funding acquisition: LC, BTK

Competing interests: Dr. Brian Kalish is on the scientific advisory board of Neuren Pharmaceuticals. However, this does not represent a conflict of interest for the current manuscript.

Data and materials availability: Source code utilized in the study can be found at https://github.com/NeuroImmuno/Placenta_MIA. All snRNAseq data generated in the project have been submitted to the Gene Expression Omnibus repository under accession number GSE315060. Reviewers can access the data using the access token cfaxssgutxybfof.

Figure 1. MIA elicits large-scale developmental abnormalities in a subset of embryos within 24 hours of poly(I:C) exposure. (A) Schematic of the maternal immune activation experimental paradigm. (B) Levels of IL-6 protein detected in the serum of dams exposed to poly(I:C) (teal) or saline (gray) measured by ELISA. Unpaired t test, ****$p < 0.0001$; n = 55 mice per condition. (C) Ratio of IL-6 levels just before and three hours after poly(I:C) injection. Unpaired t test, ****$p < 0.0001$; n = 55 mice per condition. (D) Example images of embryos harvested from dams at E13.5, 24 hours after saline or poly(I:C) exposure. Yellow arrows indicate deficits observed. Underdev., underdeveloped; mal., malformation. Scale bars, 2 mm. (E) Schematic illustrating the nomenclature used to describe different morphological dimensions of a fetus. (F)-(M) Measurement of fetal morphology and other abnormalities following poly(I:C) exposure. Parameters measured: (F) fetal weight (g); (G) Anterior-posterior diameter (mm); (H) Crown-rump length (mm); (I) Hind limb length (mm); (J) Lambda-bregma distance (mm); (K) Mandibular plane length (mm); (L) Muzzle-auricular angle (mm); (M) Percent of body covered by hemorrhages. (F)-(M) Unpaired t tests, *$p < 0.05$; **$p < 0.01$; ***$p < 0.001$; ****$p < 0.0001$. For (F), n = 63 saline and 103 poly(I:C) embryos collected from 10 and 19 distinct litters, respectively. For (G)-(H), n = 33 saline and 40 poly(I:C). For (I), n = 28 saline and 40 poly(I:C). For (J)-(L), n = 30 saline and 21 poly(I:C). For (M), n = 35 embryos of each condition. (N) Heatmap displaying the percentage of embryos exhibiting normal or abnormal development of the ear pavilion and whisker pad. Scale shown on right. (O) Heatmap displaying the percentage of embryos exhibiting normal or abnormal development of the tail and spine. Scale shown on right. For (N),(O), n = 35 embryos acquired from 6 litters per condition. (P) Percentages of saline or poly(I:C)-exposed fetuses displaying one or more developmental abnormality plotted by litter. Unpaired t test, ****$p < 0.0001$; n = 34 litters per condition.

Figure 2. MIA-induced deficits in fetal development are restricted to a subset of male embryos. (A) Images of embryos labeled based upon phenotype following MIA: poly(I:C)^{norm}, no abnormalities observed; poly(I:C)^{mod}, at least one abnormality and no signs of reabsorption observed; and poly(I:C)^{strong}, at least one abnormality and signs of reabsorption observed. Yellow arrows, underdeveloped limb and morphological abnormalities. Scale bar, 2 mm. (B) Multiple correspondence analysis (MCA) highlighting the separation of embryos into three distinct groups based upon measured phenotypes. Ellipses are centered at the group mean and oriented by the sample covariance. (C) Graph illustrating the percentage of embryos exhibiting deficits across both sexes and poly(I:C) or saline conditions. (D) Percentages of saline or poly(I:C)-exposed male and female fetuses displaying one or more developmental abnormalities plotted by litter. Two-Way ANOVA with Tukey's post test, ****$p < 0.0001$. Treatment: *$p < 0.05$; Sex: ****$p < 0.0001$; Interaction: *$p < 0.05$. (E) Schematic illustrating the organization of embryos within the womb. Embryo surrounded only by female embryos (0M), embryo surrounded by at least one male embryo (1M), and embryo surrounded by two males (2M). (F) Quantification of phenotype distribution in 0M, 1M, and 2M embryos. Statistics; **$p < 0.01$.

Figure 3. Single-nucleus RNA-sequencing unveils maternal and fetal immune activation in poly(I:C)^{mod} placentas. (A) Schematic of the tri-layered placenta with amniotic sac, amniotic fluid, and fetus shown. (B) Uniform manifold approximation and projection (UMAP) plot illustrating the 197,237 nuclei included in the single-nucleus RNA-sequencing (snRNAseq) dataset, clustered by cell type. (C) Bar graph comparing the proportion of cells belonging to each cluster in saline-treated male (gray) and poly(I:C)^{mod} (teal) placentas. Independent two-sample t tests, *$p < 0.05$. (D) Confocal images of placental sections subjected to fluorescence *in situ*

hybridization for the SpT marker *Ascl2* (yellow) with DAPI shown in cyan. D, decidua; JZ, junctional zone; arrows, TGCs. Scale bar, 50 µm. (E) Quantification of the number of TGCs per unit area in both conditions. Unpaired t test, $^{**}p < 0.05$, n=3 placentas per condition. (F) The abundance of differentially expressed genes (DEGs) between conditions for each cell type meeting a threshold of 4.0 absolute fold change and FDR < 0.05. (G) Volcano plot illustrating DEGs identified in maternally derived placental immune cells. (H) Volcano plot illustrating DEGs identified in fetally derived immune cells. (I) RNA levels of each given gene as measured by bulk RNA-sequencing of the placenta (see Figure S4), serving as validation of the snRNAseq results. (J) Volcano plot illustrating DEGs identified in decidual cells.

Figure 4. MIA reduces hormone and extracellular matrix transcripts in spongiotrophoblasts and induces a structural breakdown of the placental junctional zone. (A) Volcano plot illustrating DEGs identified in the largest cluster of spongiotrophoblasts (SpTs). (B) RNA levels of each given gene as measured by bulk RNA-sequencing of the placenta, serving as validation of the snRNAseq results. (C) Confocal images of placental sections from saline and poly(I:C)^{mod} male embryos immunostained for the collagen family member Col1a1 (magenta), DAPI shown in cyan. D, decidua; JZ, junctional zone; L, labyrinth. Arrows, examples of collagen deposition. Scale bar, 100 µm. (D) Quantification of the intensity of Col1a1 signal (A.U.) in placentas from saline and poly(I:C)^{mod} male embryos. Unpaired t test, $^{*}p < 0.05$; n = 3 placentas per condition. (E) Dot plot illustrating changes in genes involved in hormone biosynthesis, signaling, and detection following MIA based upon snRNAseq. Fold change and statistical significance scales given on the right. (F) Volcano plot illustrating DEGs identified in SpT$_{MIA}$ cells. (G) Levels of *Ceacam9* RNA in saline and poly(I:C)^{mod} placentas based upon bulk RNA-sequencing. Unpaired t test, $^{*}p < 0.05$; n = 4 placentas per condition. (H) Microscopy images of H&E-stained placentas from male mice across conditions and phenotypes. D, decidua; JZ, junctional zone; L, labyrinth. Arrows, necrosis or degeneration. Asterisks, hemorrhagic congestion. Scale bar, 500 µm. Inset scale bar, 100 µm. (I),(J) Pathological scoring of degenerative signatures in male placentas based upon H&E staining. (I) Decidual degeneration. (J) trophoblast necrosis. (I),(J) One-way ANOVA with Tukey's post test. $^{*}p < 0.05$; $^{***}p < 0.001$; and $^{****}p < 0.0001$. For (I), n = 11 saline and 6 poly(I:C)^{norm}, 14 poly(I:C)^{mod}, and 10 poly(I:C)^{strong}. For (J), n = 13 saline, 8 poly(I:C)^{norm}, 13 poly(I:C)^{mod}, and 10 poly(I:C)^{strong}.

Figure 5. Innate and adaptive immune cells and pro-inflammatory cytokines infiltrate the amniotic fluid following MIA. (A) Heatmap demonstrating the abundance of distinct populations of immune cells in the amniotic fluid (AF) of individual embryos across sexes, conditions, and phenotypes. Rows, cell types given on left of heatmap. Columns, sex and condition. Scale on right. Red box emphasizes robust changes in NK and T cells in affected male placentas. (B)-(E) Quantification of the relative abundance (percentage of parental gate) of major immune cell populations in the AF: (B) monocytes/macrophages; (C) Natural killer (NK) cells; (D) Dendritic cells (DCs); and (E) T cells. For (B)-(E) One-way ANOVA with Tukey's post test; $^{*}p < 0.05$; $^{**}p < 0.01$; $^{***}p < 0.001$; and $^{****}p < 0.0001$; n = 5 saline and poly(I:C)^{norm}, n = 6 poly(I:C)^{mod}, and n = 4 poly(I:C)^{strong} embryos collected from 5 litters per condition. (F) tSNE maps of immune cell abundance across saline and poly(I:C) conditions plotted by phenotype. Each map was derived from a single embryo and poly(I:C)-treated conditions were present in the same litter. (G) Heatmap demonstrating the induction of pro-inflammatory cytokines in the AF following MIA, scale shown on right.

Figure 6. IL-6 is required for MIA-driven developmental abnormalities in male embryos. (A) IL-6 protein levels measured within the AF of male and female embryos from saline and poly(I:C) treatment groups. Two-Way ANOVA with Tukey's post test, ****$p < 0.0001$; n = 10 saline female, 13 saline male, 6 poly(I:C) female, and 13 poly(I:C) male embryos. (B) IL-6 protein levels measured across male embryos of each phenotype. One-Way ANOVA with Tukey's post test; **$p < 0.01$; ***$p < 0.001$; n = 13 saline, 12 poly(I:C)^{norm}, 13 poly(I:C)^{mod}, and 10 poly(I:C)^{strong} embryos. (C) Levels of IL-6 protein detected in the serum of dams exposed to poly(I:C) (teal), poly(I:C) and MP5-30 (indigo), or saline (gray) measured by ELISA. Unpaired t test, ****$p < 0.0001$; n = 4 litters per condition. (D) Analysis of IL-6 in the AF of embryos across conditions, demonstrating depletion of IL-6 in the AF of MP5-30-exposed embryos. One-way ANOVA with Tukey's post test; **$p < 0.01$; ***$p < 0.001$; n = 15 saline, 6 poly(I:C)^{norm}, 8 poly[I:C]^{mod}, 4 poly[I:C]^{strong}, and 18 MP5-30 + poly(I:C). (E) Example images of fetuses from each treatment group at E13.5. Scale bars, 1 mm. (F)-(J) Measurement of fetal morphology across conditions. Parameters measured: (F) fetal weight (g); (G) Crown-rump length (mm); (H) Anterior-posterior diameter (mm); (I) Mandibular plane length (mm); and (J) lambda-bregma distance (mm). One-way ANOVAs with Tukey's post test, **$p < 0.01$; ***$p < 0.001$; ****$p < 0.0001$. For (F), n = 15 saline, 16 poly(I:C), and 16 MP5-30 + poly(I:C) embryos. For (G), n = 18 saline, 13 poly(I:C), and 18 MP5-30 + poly(I:C) embryos. For (H), n = 18 saline, 12 poly(I:C), and 18 MP5-30 + polyI:C) embryos. For (I), n = 16 saline, 13 poly(I:C), and 16 MP5-30 + poly(I:C). For (J), n = 17 saline, 13 poly(I:C), and 18 MP5-30 + poly(I:C) embryos.

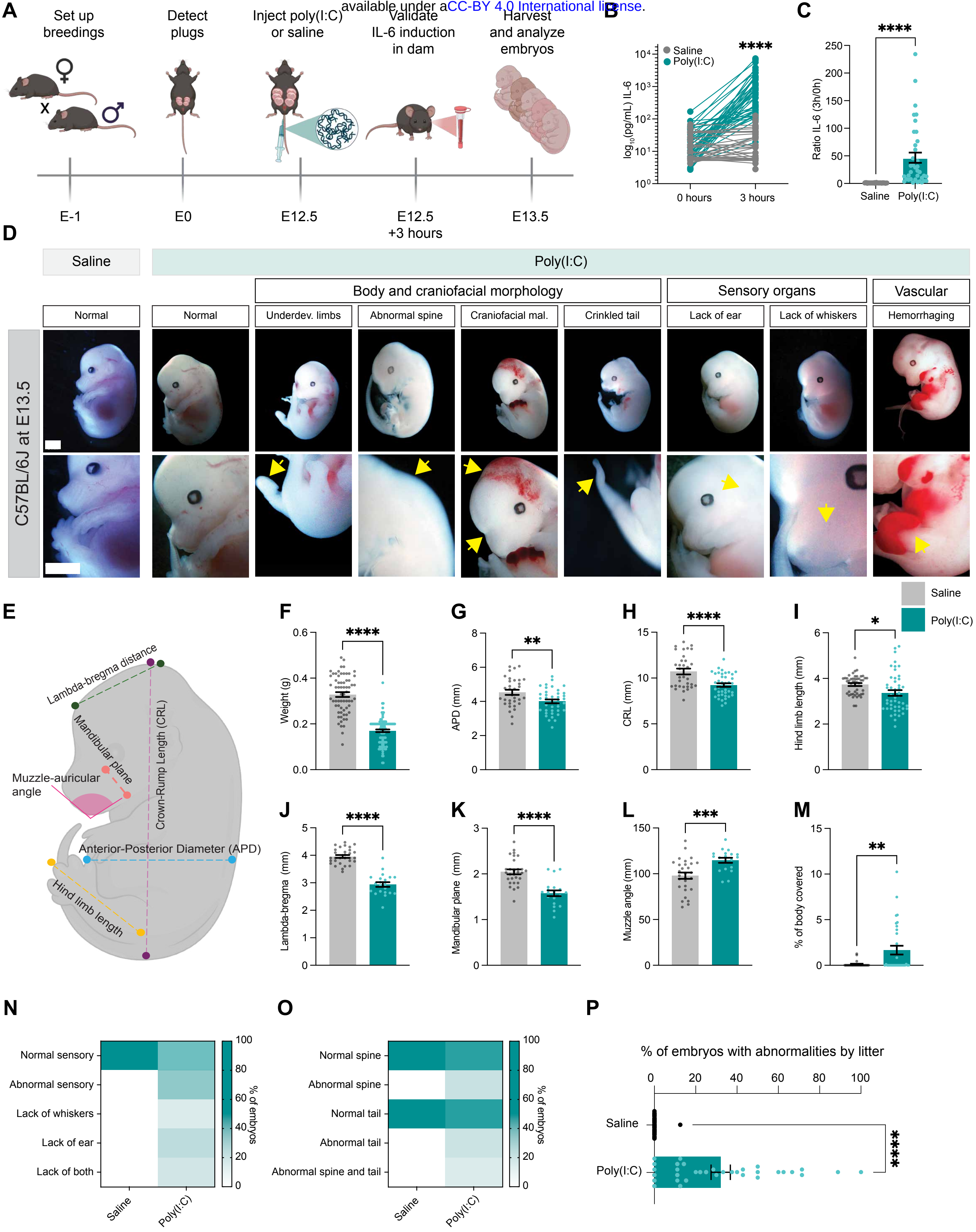
A
Set up breedings
Detect plugs
Inject poly(I:C) or saline
Validate IL-6 induction in dam
Harvest and analyze embryos
♀
X
♂
E-1
E0
E12.5
E12.5 +3 hours
E13.5
B
Saline
Poly(I:C)
****
$\log_{10}$(pg/mL) IL-6
10^4
10^3
10^2
10^1
10^0
0 hours
3 hours
C
****
Ratio IL-6 (3h/0h)
250
200
150
100
50
0
Saline
Poly(I:C)
D
Saline
Poly(I:C)
Body and craniofacial morphology
Sensory organs
Vascular
Normal
Normal
Underdev. limbs
Abnormal spine
Craniofacial mal.
Crinkled tail
Lack of ear
Lack of whiskers
Hemorrhaging
C57BL/6J at E13.5
E
Lambda-bregma distance
Mandibular plane
Muzzle-auricular angle
Crown-Rump Length (CRL)
Anterior-Posterior Diameter (APD)
Hind limb length
F
****
Weight (g)
0.6
0.4
0.2
0.0
G
**
APD (mm)
8
6
4
2
0
H
****
CRL (mm)
15
10
5
0
I
*
Hind limb length (mm)
6
4
2
0
Saline
Poly(I:C)
J
****
Lambda-bregma (mm)
5
4
3
2
1
0
K
****
Mandibular plane (mm)
3
2
1
0
L
***
Muzzle angle (mm)
150
100
50
0
M
**
% of body covered
15
10
5
0
N
Normal sensory
Abnormal sensory
Lack of whiskers
Lack of ear
Lack of both
Saline
Poly(I:C)
100
80
60
40
20
0
% of embryos
O
Normal spine
Abnormal spine
Normal tail
Abnormal tail
Abnormal spine and tail
Saline
Poly(I:C)
100
80
60
40
20
0
% of embryos
P
% of embryos with abnormalities by litter
0
20
40
60
80
100
Saline
Poly(I:C)
****

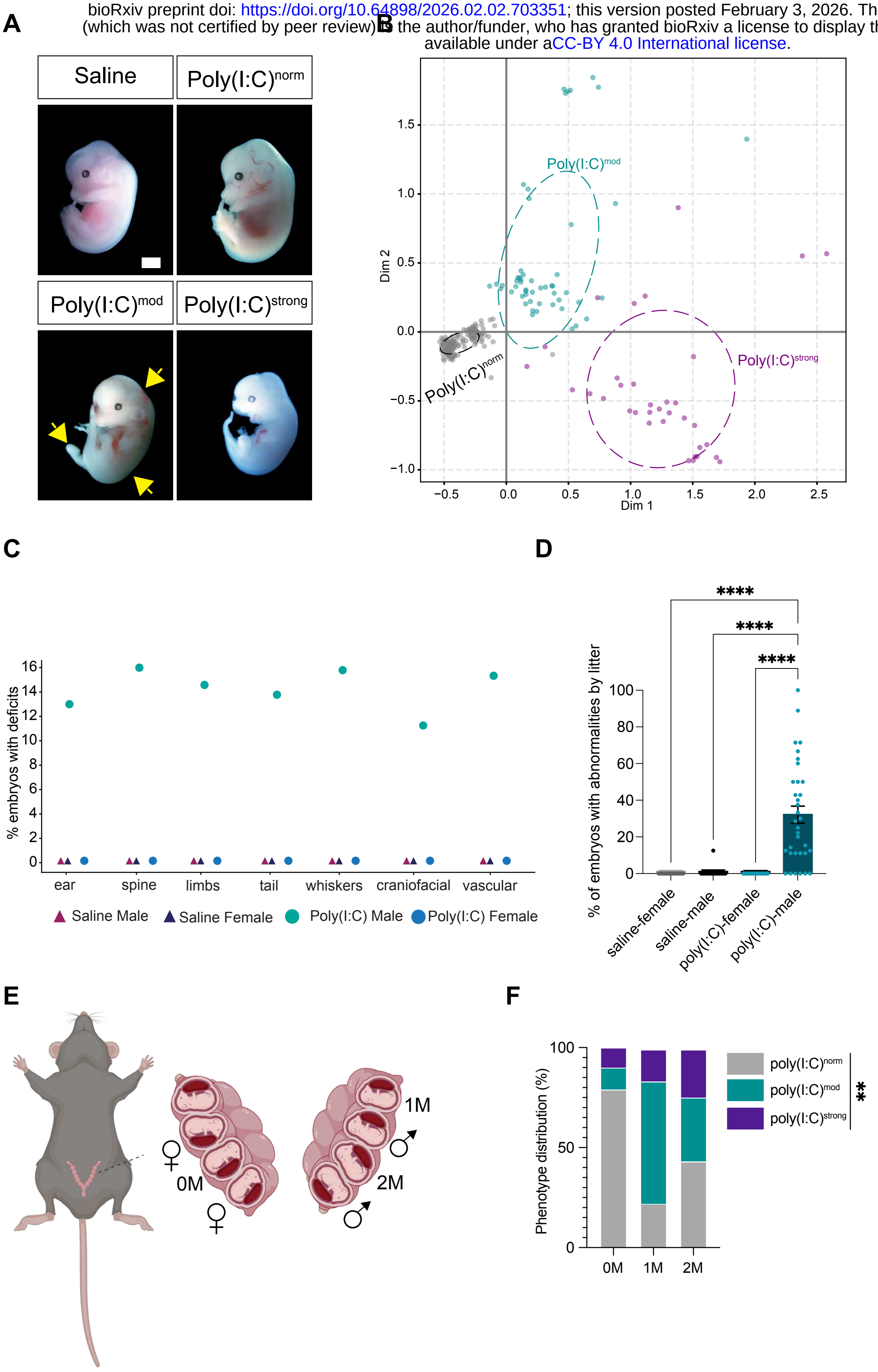
A
Saline
Poly(I:C)^{norm}
Poly(I:C)^{mod}
Poly(I:C)^{strong}
B
Poly(I:C)^{mod}
Poly(I:C)^{strong}
Poly(I:C)^{norm}
Dim 2
Dim 1
1.5
1.0
0.5
0.0
−0.5
−1.0
−0.5
0.0
0.5
1.0
1.5
2.0
2.5
C
% embryos with deficits
16
14
12
10
8
6
4
2
0
ear
spine
limbs
tail
whiskers
craniofacial
vascular
Saline Male
Saline Female
Poly(I:C) Male
Poly(I:C) Female
D
****
****
****
% of embryos with abnormalities by litter
100
80
60
40
20
0
saline-female
saline-male
poly(I:C)-female
poly(I:C)-male
E
♀
0M
♀
1M
♂
2M
♂
F
Phenotype distribution (%)
100
50
0
0M
1M
2M
poly(I:C)^{norm}
poly(I:C)^{mod}
poly(I:C)^{strong}
**

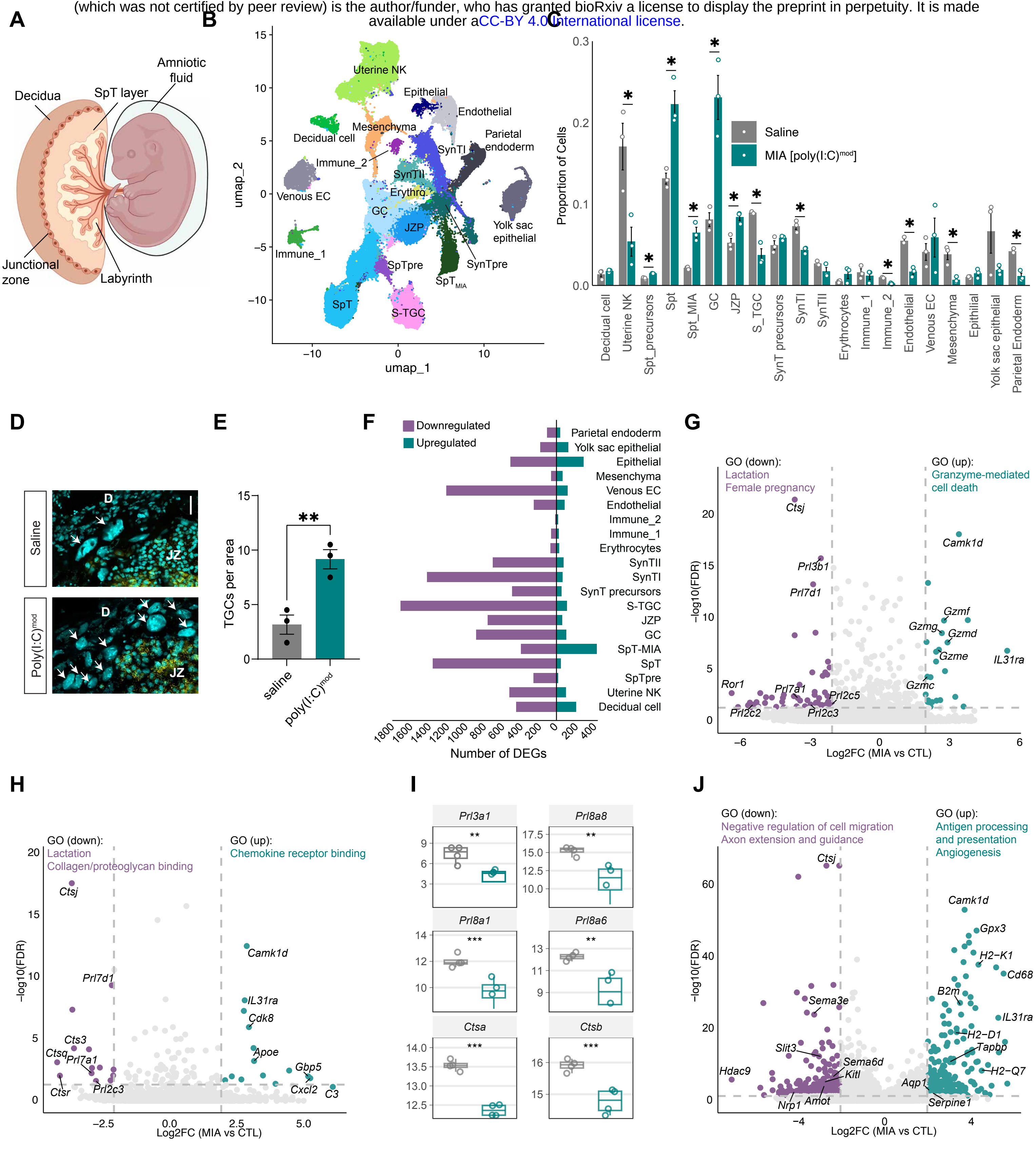
A
Amniotic fluid
Decidua
SpT layer
Junctional zone
Labyrinth
B
Uterine NK
Epithelial
Endothelial
Mesenchyma
Decidual cell
Parietal endoderm
SynTI
Immune_2
SynTII
Venous EC
Erythro.
GC
JZP
Yolk sac epithelial
Immune_1
SpTpre
SynTpre
SpT_MIA
SpT
S-TGC
umap_1
umap_2
C
Proportion of Cells
Saline
MIA [poly(I:C)^mod]
Decidual cell
Uterine NK
Spt_precursors
Spt
Spt_MIA
GC
JZP
S_TGC
SynT precursors
SynTI
SynTII
Erythrocytes
Immune_1
Immune_2
Endothelial
Venous EC
Mesenchyma
Epithilial
Yolk sac epithelial
Parietal Endoderm
D
Saline
Poly(I:C)^mod
D
JZ
E
TGCs per area
**
saline
poly(I:C)^mod
F
Downregulated
Upregulated
Parietal endoderm
Yolk sac epithelial
Epithelial
Mesenchyma
Venous EC
Endothelial
Immune_2
Immune_1
Erythrocytes
SynTII
SynTI
SynT precursors
S-TGC
JZP
GC
SpT-MIA
SpT
SpTpre
Uterine NK
Decidual cell
Number of DEGs
G
GO (down):
Lactation
Female pregnancy
GO (up):
Granzyme-mediated cell death
Ctsj
Camk1d
Prl3b1
Prl7d1
Gzmf
Gzmg
Gzmd
Gzme
IL31ra
Ror1
Prl7a1
Gzmc
Prl2c5
Prl2c2
Prl2c3
-log10(FDR)
Log2FC (MIA vs CTL)
H
GO (down):
Lactation
Collagen/proteoglycan binding
GO (up):
Chemokine receptor binding
Ctsj
Camk1d
Prl7d1
IL31ra
Cdk8
Cts3
Apoe
Ctsq
Prl7a1
Gbp5
Ctsr
Prl2c3
Cxcl2
C3
-log10(FDR)
Log2FC (MIA vs CTL)
I
Prl3a1
Prl8a8
Prl8a1
Prl8a6
Ctsa
Ctsb
**
***
J
GO (down):
Negative regulation of cell migration
Axon extension and guidance
GO (up):
Antigen processing and presentation
Angiogenesis
Ctsj
Camk1d
Gpx3
H2-K1
Cd68
B2m
Sema3e
IL31ra
H2-D1
Tapbp
Slit3
Sema6d
Hdac9
Kitl
H2-Q7
Aqp1
Nrp1
Amot
Serpine1
-log10(FDR)
Log2FC (MIA vs CTL)

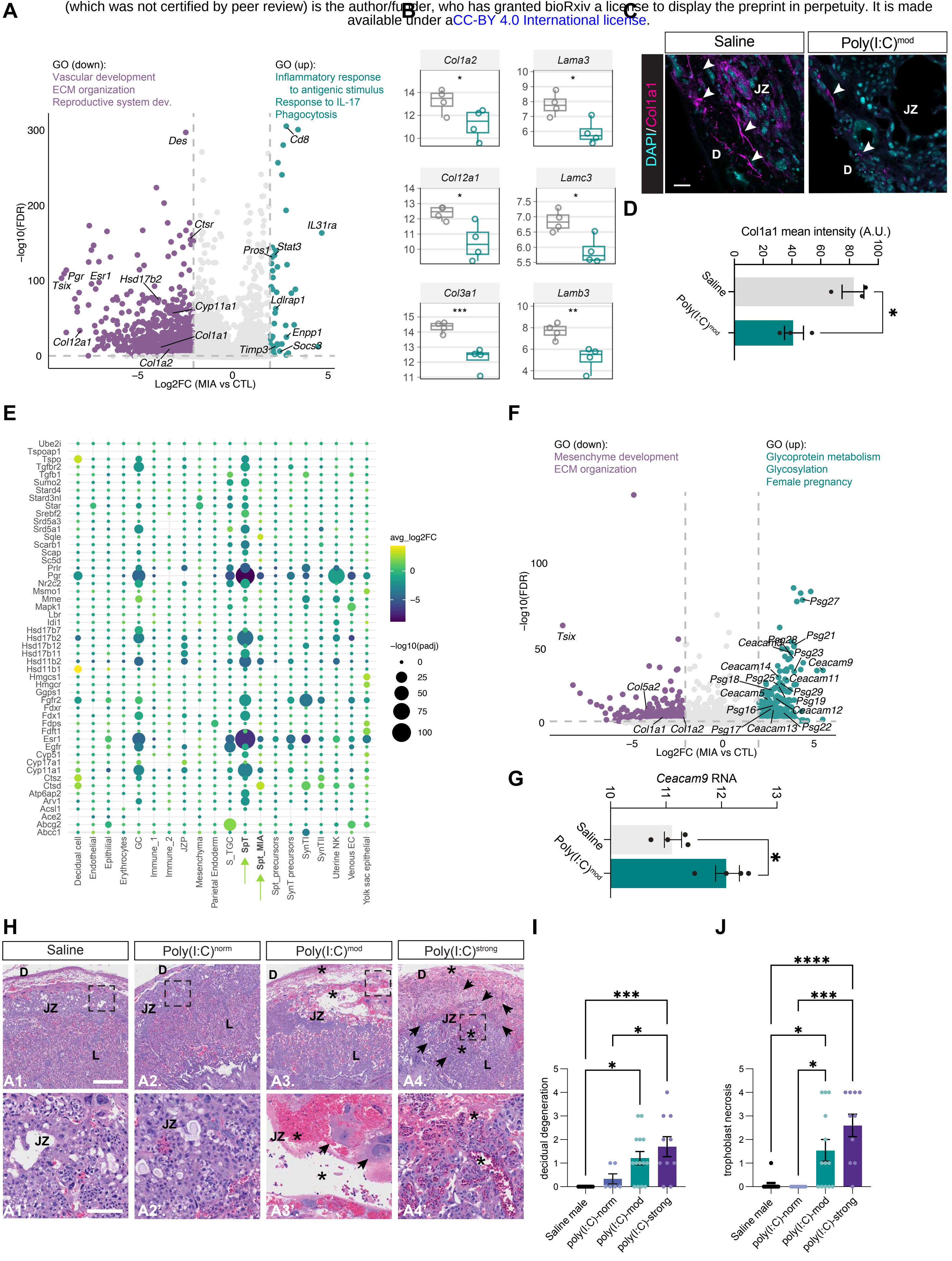
A
GO (down):
Vascular development
ECM organization
Reproductive system dev.
GO (up):
Inflammatory response to antigenic stimulus
Response to IL-17
Phagocytosis
-log10(FDR)
Log2FC (MIA vs CTL)
Des
Cd8
IL31ra
Ctsr
Pros1
Stat3
Pgr
Esr1
Tsix
Hsd17b2
Cyp11a1
Ldlrap1
Col12a1
Col1a1
Enpp1
Timp3
Socs3
Col1a2
B
Col1a2
Lama3
Col12a1
Lamc3
Col3a1
Lamb3
*
***
**
C
Saline
Poly(I:C)mod
DAPI/Col1a1
JZ
D
D
Col1a1 mean intensity (A.U.)
Saline
Poly(I:C)mod
*
E
Ube2i
Tspoap1
Tspo
Tgfbr2
Tgfb1
Sumo2
Stard4
Stard3nl
Star
Srebf2
Srd5a3
Srd5a1
Sqle
Scarb1
Scap
Sc5d
Prlr
Pgr
Nr2c2
Msmo1
Mme
Mapk1
Lbr
Idi1
Hsd17b7
Hsd17b2
Hsd17b12
Hsd17b11
Hsd11b2
Hsd11b1
Hmgcs1
Hmgcr
Ggps1
Fgfr2
Fdxr
Fdx1
Fdps
Fdft1
Esr1
Egfr
Cyp51
Cyp17a1
Cyp11a1
Ctsz
Ctsd
Atp6ap2
Arv1
Acsl1
Ace2
Abcg2
Abcc1
Decidual cell
Endothelial
Epithilial
Erythrocytes
GC
Immune_1
Immune_2
JZP
Mesenchyma
Parietal Endoderm
S_TGC
SpT
Spt_MIA
Spt_precursors
SynT precursors
SynTII
SynTII
Uterine NK
Venous EC
Yolk sac epithelial
avg_log2FC
0
-5
-log10(padj)
0
25
50
75
100
F
GO (down):
Mesenchyme development
ECM organization
GO (up):
Glycoprotein metabolism
Glycosylation
Female pregnancy
-log10(FDR)
Log2FC (MIA vs CTL)
Psg27
Tsix
Psg28
Psg21
Ceacam3
Psg23
Ceacam9
Ceacam14
Psg18
Psg25
Ceacam11
Col5a2
Ceacam5
Psg29
Psg19
Psg16
Ceacam12
Col1a1
Col1a2
Psg17
Ceacam13
Psg22
G
Ceacam9 RNA
Saline
Poly(I:C)mod
*
H
Saline
Poly(I:C)norm
Poly(I:C)mod
Poly(I:C)strong
D
JZ
L
A1.
A2.
A3.
A4.
A1'.
A2'.
A3'.
A4'.
I
decidual degeneration
Saline male
poly(I:C)-norm
poly(I:C)-mod
poly(I:C)-strong
***
*
*
J
trophoblast necrosis
****
***
*
*

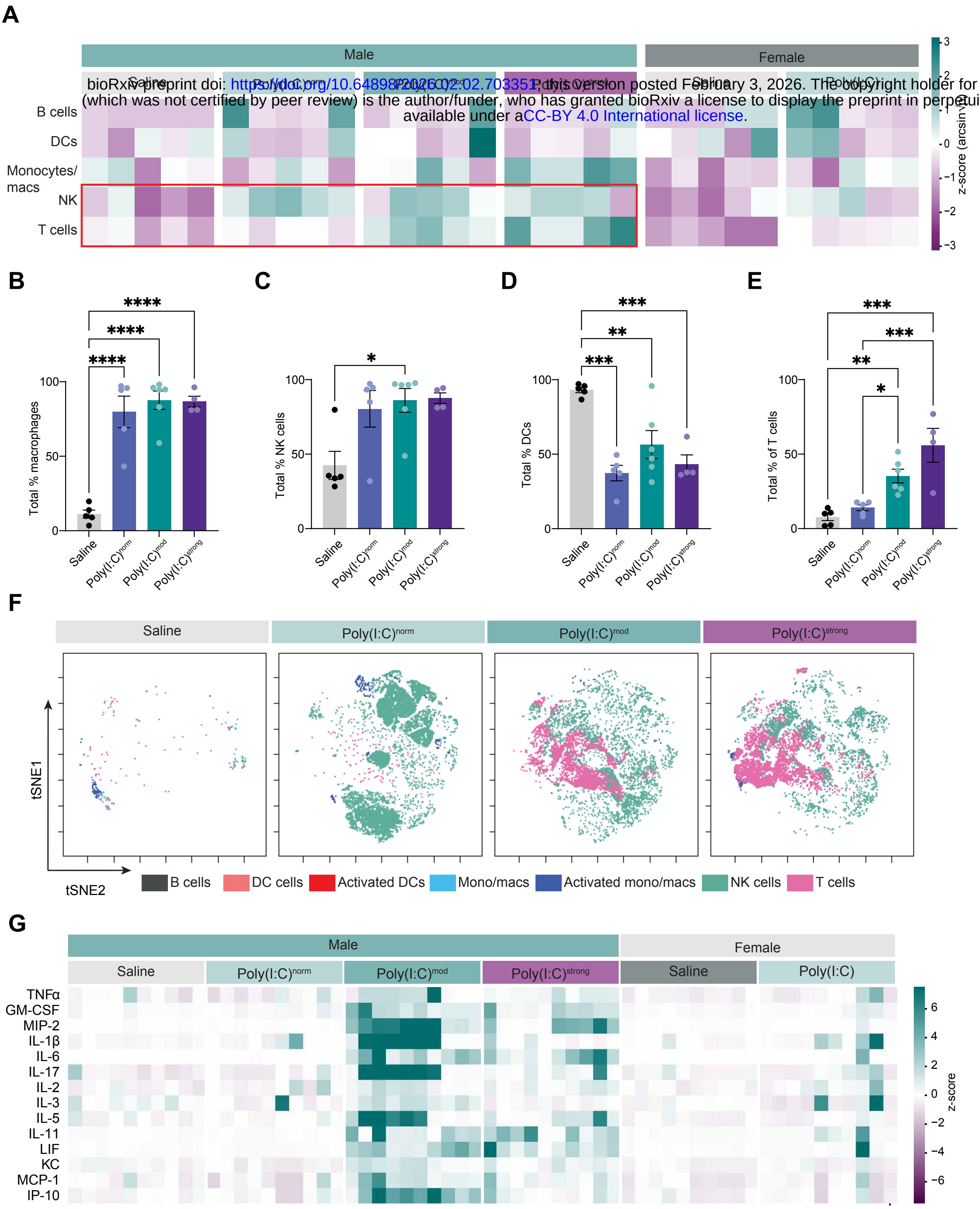
A
Male
Female
Saline
Poly(I:C)norm
Poly(I:C)mod
Poly(I:C)strong
Saline
Poly(I:C)
B cells
DCs
Monocytes/macs
NK
T cells
z-score (arcsin√)
3
2
1
0
−1
−2
−3
B
Total % macrophages
****
****
****
C
Total % NK cells
*
D
Total % DCs
***
**
***
E
Total % of T cells
***
***
**
*
0
50
100
Saline
Poly(I:C)norm
Poly(I:C)mod
Poly(I:C)strong
F
Saline
Poly(I:C)norm
Poly(I:C)mod
Poly(I:C)strong
tSNE1
tSNE2
B cells
DC cells
Activated DCs
Mono/macs
Activated mono/macs
NK cells
T cells
G
Male
Female
Saline
Poly(I:C)norm
Poly(I:C)mod
Poly(I:C)strong
Saline
Poly(I:C)
TNFα
GM-CSF
MIP-2
IL-1β
IL-6
IL-17
IL-2
IL-3
IL-5
IL-11
LIF
KC
MCP-1
IP-10
z-score
6
4
2
0
−2
−4
−6

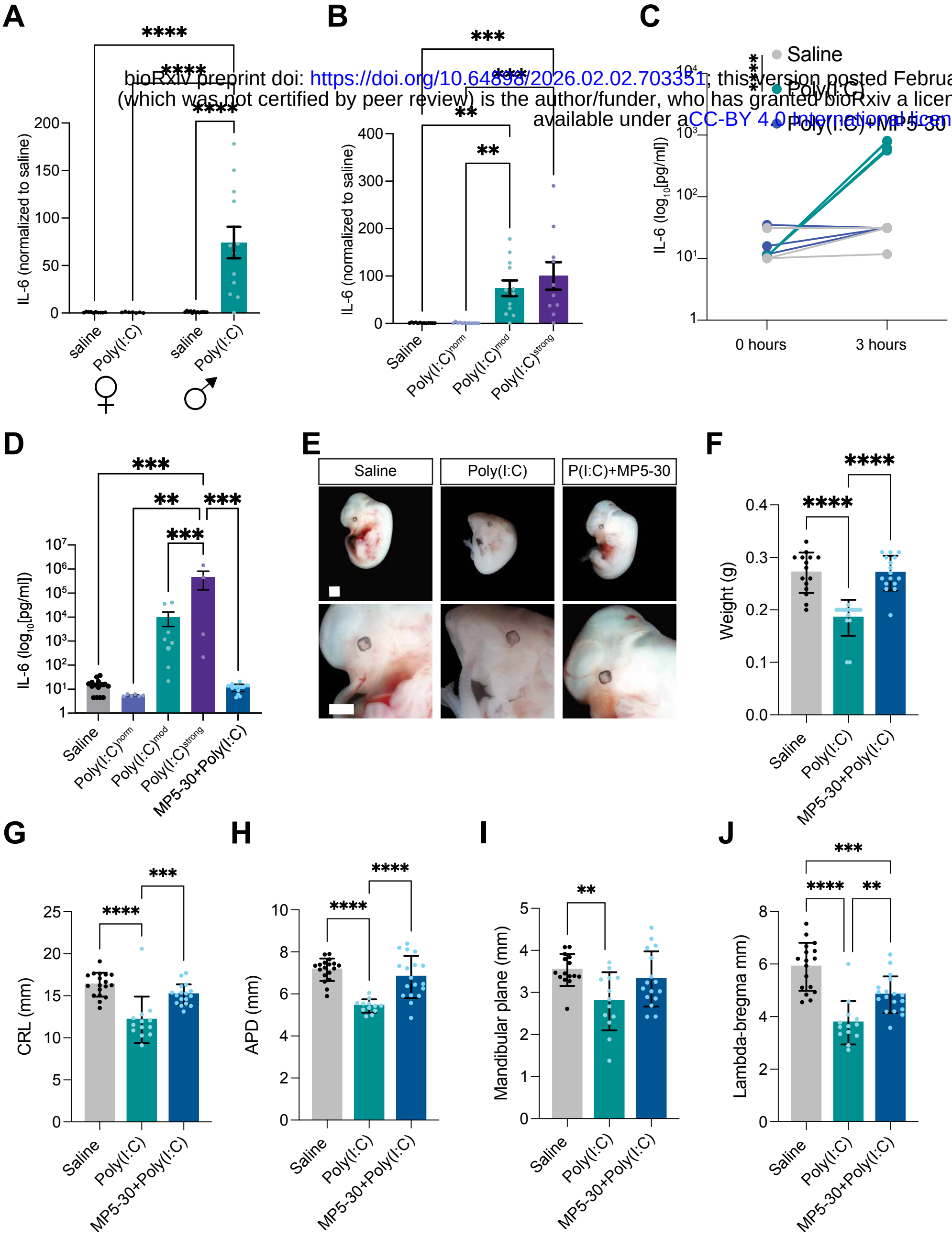
A
IL-6 (normalized to saline)
0
50
100
150
200
saline
Poly(I:C)
saline
Poly(I:C)
♀
♂
****
****
****
B
IL-6 (normalized to saline)
0
100
200
300
400
Saline
Poly(I:C)norm
Poly(I:C)mod
Poly(I:C)strong
***
***
**
**
C
Saline
Poly(I:C)
Poly(I:C)+MP5-30
IL-6 (log10[pg/ml])
1
10¹
10²
10³
10⁴
0 hours
3 hours
****
D
IL-6 (log10[pg/ml])
1
10¹
10²
10³
10⁴
10⁵
10⁶
10⁷
Saline
Poly(I:C)norm
Poly(I:C)mod
Poly(I:C)strong
MP5-30+Poly(I:C)
***
**
***
***
E
Saline
Poly(I:C)
P(I:C)+MP5-30
F
Weight (g)
0.0
0.1
0.2
0.3
0.4
Saline
Poly(I:C)
MP5-30+Poly(I:C)
****
****
G
CRL (mm)
0
5
10
15
20
25
Saline
Poly(I:C)
MP5-30+Poly(I:C)
****
***
H
APD (mm)
0
2
4
6
8
10
Saline
Poly(I:C)
MP5-30+Poly(I:C)
****
****
I
Mandibular plane (mm)
0
1
2
3
4
5
Saline
Poly(I:C)
MP5-30+Poly(I:C)
**
J
Lambda-bregma mm)
0
2
4
6
8
Saline
Poly(I:C)
MP5-30+Poly(I:C)
***
****
**